,,
,,,

Masters Thesis

Jacob Bundgaard Nielsen

Heavy Neutral Lepton Detection in the Tau Channel

Supervisor : Stefania Xella

Handed in: 15/3-2021

Abstract

Neutrinos are the least understood of all particles in the Standard Model. In particular, it is unknown how they acquire a non-zero mass. Some theories, invoking a see saw mechanism, require the existence of new heavy neutral leptons, to give mass to neutrinos. A search for a heavy neutral lepton (HNL), also referred to as N's is performed using simulated data from the ATLAS detector at the LHC at $\sqrt{s}$=13 TeV, and the sensitivity studied for an integrated luminosity of 140 fb^1 (corresponding to the data collected in LHC Run 2). The N's are particles of the νMSM, which is a potential extension to the Standard Model, aiming to explain several beyond Standard Model phenomena. This search focuses on the so called opposite sign or same sign, different flavour, channels, sensitive to prompt production channels $W^{\pm} \rightarrow \mu^{\pm} \tau^{\pm} e^{\mp} \nu_e$ and $W^{\pm} \rightarrow \mu^{\pm} \tau^{\mp} e^{\pm} \bar{\nu}_e$ respectively, where a selection strategy for the detection of N's is proposed. This search is conducted at two different prospective mass points for the N's with m_N=20 GeV and m_N=50 GeV.

This search obtains a $\frac{S}{\sqrt{B}} \approx 0.01$ which is insufficient to make a discovery, leading to the conclusion that the tau channel might not be a viable candidate for the discovery of mixing of the N's with the tau neutrino flavour.

The selection applied in this search is not fully optimized, meaning that there is still more work to be done on the channel for future searches.

Acknowledgements

Contents

Introduction

The Standard Model (SM) has proven successful in describing a broad range of phenomena, however there are still many physical observations which can not be explained through the SM in it's current form. Some of such unexplained phenomena are the nature of dark matter, the minuscule masses of the SM neutrinos, the fact that neutrinos have masses at all and the Baryon asymmetry of the universe.

Several theories have been put forward in an attempt to explain these phenomena by extending the SM with new particle fields. One such model is the so called "neutrino minimal SM" (νMSM), this model explains these phenomena by adding three heavy right-handed neutral leptons to the SM, which explains all of these beyond SM phenomena without adding any new introducing any new energy scales. In this νMSM the small neutrino masses are explained via the see-saw mechanism with the new heavy neutral leptons (HNLs) generally referred to as N's. The lightest of the three N's provides a dark matter candidate, and has a mass way below what can be observed at the LHC, and no chance of being detected there. The Baryon asymmetry of the universe is explained provided that the two heavier N's have degenerate masses, below the W mass. This effectively means there is perhaps one new neutrino observable at the LHC.

The N's are produced through mixing with the SM neutrinos, this mixing will be governed by a coupling defined by the mixing angle V_{lN}, where l denotes the flavor of the active neutrino and N denotes the new heavy neutrino. This mixing would be rare, so in order to study it, it is crucial to have a very large amount of data, as well as a fairly efficient process for signal selection. Limits have been set on this mixing angle first at LEP, which have since been improved upon by different experiments including the ATLAS experiment at the LHC. The mass and coupling of the heavy neutral leptons both influence the lifetime of the heavy neutral lepton, and therefore how far they propagate within the detector before decaying.

In this thesis a search for Ns is conducted using the ATLAS detector at the CERN Large Hadron Collider (LHC). It uses simulated data corresponding to what has been collected in the years 2015-2017 at a centre-of-mass energy of $\sqrt{s}$=13 TeV and corresponds to an integrated luminosity of 140 fb-1. The N mass is restricted to be below the W mass, and the search exploits the large production of W bosons at LHC. The search focuses on the prompt $pp \rightarrow W^{\pm} \rightarrow \mu^{\pm}\tau^{\pm}e^{\mp}$ channel and the $W^{\pm} \rightarrow \mu^{\pm}\tau^{\mp}$ e$^{\pm}$ channel. Both channels are possible manifestations of the presence of a new right–handed neutrino in Nature, which can manifest as either Majorana or quasi-Dirac particle depending on the relation between the degeneracy in mass and the total decay width of the two heaviest N's in the νMSM. The choice of τ leptons is due to the complete absence of knowledge on the mixing of the N's to tau neutrinos from LHC data to this date.

This thesis consists of the following sections. Section 2 describes the relevant theory behind the existence of Heavy Neutral Leptons. Section 3 provides an introduction to the ATLAS experiment and its different detectors. Section 4 describes the basic concepts needed to define the analysis. Section 5 provides an explanation for the specific choice of channel that this thesis works with. Section 6 goes into how data analysis was carried out along with the results of said data analysis. In section 7 an outline for potential future improvements to this analysis is presented.

This thesis looks into which tau channel is the most feasible to analyse at ATLAS in order to probe the mixing with N's. As well as formulating a basic selection strategy for separating this signal from the relevant backgrounds. With this selection a $\frac{S}{\sqrt{B}} \approx 0.01$, which is insufficient to make a discovery, but could be improved with additional tuning of the selection strategy.

Theory

In this section I will introduce the Standard Model (SM) theory of particle physics and the extension needed to introduce heavy neutral leptons, as well as how heavy neutral leptons have been searched so far in experiments.

The Standard Model

The SM is a theory which gathers all known information about the different fundamental forces and particles into one comprehensive theory which can explain all known particle physics phenomena. The theory has been hugely successful in both describing known phenomena as well as predicting new particles such as the Higgs boson. The theory is often visually represented by Figure 1 which is split into three categories of the particles which make up all matter in the form of leptons and quarks, and the force carrying gauge bosons.
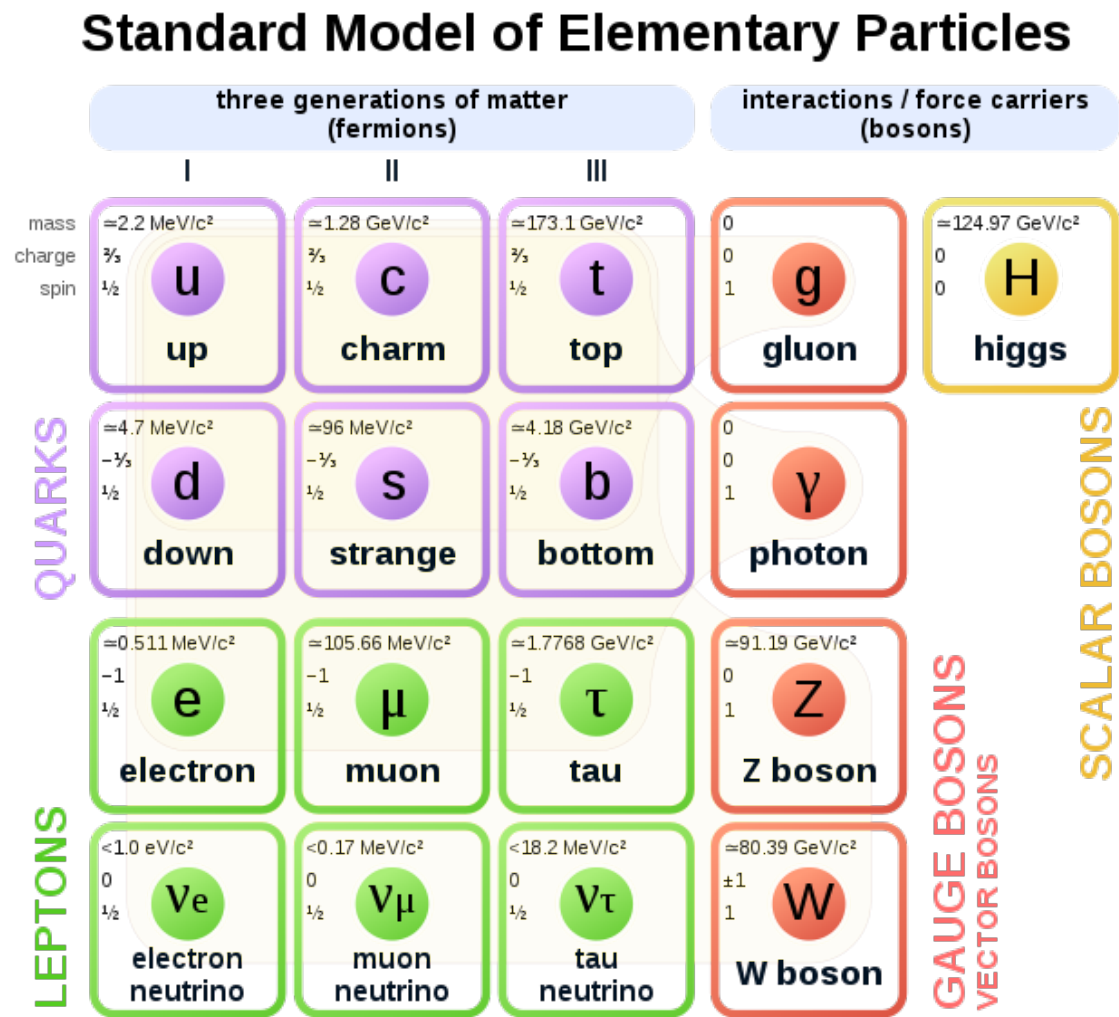
Figure 1: Visualization of the SM of elementary particles. From [1], under creative commons license CC-BY[2], adapted to natural units.

Each particle of the SM has fundamental properties, as shown in Figure 1, such as mass, charge, and spin. Half integer spin particles are called fermions, and are the matter constituents. Integer spin particles are called bosons, and are force constituents (W,Z,H,gluons,photon). The SM is formulated as a renormalisable Quantum Field Theory (QFT) based on the $SU(3) \times SU(2) \times U(1)$ gauge group.

Helicity and Chirality

Helicity Helicity is an observable quality of particles which measures the angle between the direction of the particles momentum and the spin of the particle given as: $H = \sigma \times p$ where both variables are unit vectors representing the direction of spin and momentum respectively. Positive (or right-handed) helicity corresponds to the spin being parallel to the momentum, and conversely negative (or left-handed) helicity corresponds to spin being in the opposite direction compared to momentum. Due to this definition of helicity if parity was conserved we would expect the expectation value helicity to be equal to zero as we wouldn't expect any helicity to be favoured in random decays if parity was conserved. This was however shown not to be the case, first in the 1957 experiment mentioned later and as seen in [3], and in several other experiments since then.

Chirality Unlike helicity, chirality is an operator used in particle physics without any direct physical interpretation. Although chirality isn't an intuitive physical property, it is connected with pure right or left handed helicity eigenstates, as those helicity eigenstates are also chiral eigenstates for massless particles or for sufficiently relativistic particles (E»m). Although helicity is subject to the chosen reference frame, chirality is an intrinsic property of the particle which is independent of the chosen reference frame. Matter particles (fermions) in the SM are described via right-handed or left-handed chiral fields.

The Higgs mechanism

In the SM all particles are described by quantum fields. In its original formulation, the SM contained massless fields. In order for the SM to account for the masses of particles, a field was introduced in the theory, the Higgs field, which interacts with the SM particles via so called Yukawa coupling constants. Through such interactions the quarks and leptons gain their masses. In order to understand the origin of mass via the Higgs field, we need to introduce what is called "spontaneous symmetry breaking". If we introduce a scalar doublet Higgs field:

$$\phi = \begin{pmatrix} \phi^+ \\ \phi^0 \end{pmatrix}, \tag{1}$$

The scalar field then has a potential of the form:

$$U(\phi) = \mu^2 \phi^\dagger \phi + \gamma(\phi^\dagger \phi)^2, \gamma \in \mathbb{R}_+ \tag{2}$$

with the lagrangian:

$$\mathcal{L} = (\partial_\mu \phi) * (\partial^\mu \phi) - U(\phi) \tag{3}$$

The field will have its minimum at:

$$\langle \phi \rangle = \frac{|\mu|}{\sqrt{\gamma}} = v \tag{4}$$

for imaginary values of μ, $U(\phi)$ will be symmetric on both ϕ's real and imaginary parts, thus the minimum will be degenerate and satisfy:

$$\phi\phi^\dagger = \frac{v^2}{2} \tag{5}$$

When one of these degenerate vacuum states is chosen in Nature, during a phase transition, that is what is called spontaneous symmetry breaking. Mass in the SM is explained through Yukawa couplings with the Higgs boson in spontaneous electroweak symmetry breaking with a non-zero expectation value of v.

This spontaneous symmetry breaking acts differently on different type of particles (fermions and bosons), so we will explain each one at the time.

Electroweak gauge bosons The electroweak force requires invariance of the lagrangian on the $SU(2)_L$ x $U(1)_Y$ local gauge symmetry of the SM. However left-handed particles transform as weak isospin doublets, right-handed particles transform as singlets, and an explicit mass term in the lagrangian would break down this invariance. Therefore the bosons mediating the electroweak force should be massless. But we know they are not, as the mass of the W boson is $80.39\ GeV/c^2$ and the Z boson's mass is $91.19\ GeV/c^2$, as reported in Figure 1. If we add the complex scalar field from eq. 1 to the lagrangian describing electroweak interactions between fermions, and we require it to be gauge invariant, as spontaneous symmetry breaking happens, we get a mass term from the SM gauge bosons interaction with the Higgs field.

We describe the symmetry breaking by choosing the expression for the scalar field to be:

$$\phi = \frac{1}{\sqrt{2}} \begin{pmatrix} 0 \\ v + h(x) \end{pmatrix} \tag{6}$$

From this choice, the lagrangian after symmetry breaking contains interactions of the Higgs field with electroweak bosons (terms containing $h(x)$) and mass terms for the bosons (terms containing v). The W boson mass term is

$$m_W = \frac{1}{2} g_W v \tag{7}$$

where g_W is the weak interaction coupling constant or interaction strength, and the Z mass term is

$$m_Z = \frac{1}{2} \frac{g_W}{cos\theta_W} v. \tag{8}$$

where $tan\theta_W = \frac{g'}{g_W}$, and g' is the electromagnetic interaction coupling constant.

Fermions The Yukawa coupling constant or interaction strength of the Higgs field to fermions is what gives fermions their mass. When electroweak symmetry is broken, see 6, the Yukawa couplings are connected to the masses of the particles in the generations i and j by

$$Y_{ij}^u v = (m_u)_{ij}, \quad Y_{ij}^d v = (m_d)_{ij}, \quad Y_{ij}^e v = (m_e)_{ij} \tag{9}$$

where $(m_{u,d,e})_{ij}$ denotes the masses of the up- and down-type quarks and e denotes the charged leptons. Remarkably there is no mass term for neutrinos in the lagrangian, which, given the observational properties we are about to list, is one of the major limitations for the SM. We will describe how to rectify the SM with some additions later, in the sections about the seesaw mechanism and νMSM.

Neutrinos

It is well established through experimental evidence that SM neutrinos only exist in left-handed chiral states, and right-handed chiral states for anti-neutrinos, and we will look into this experimental evidence next. The interaction with the Higgs field switches the chirality of a particle, meaning that if we only have left-handed neutrinos then they cannot have mass according to the SM, and indeed they are included in the SM as being massless particles. Although neutrinos are massless according to the SM more recent observations have put this into question, one such observation is the existence of neutrino oscillations which will be explained in some detail in a later section.

Chiral left handedness of SM neutrinos

An experiment done in 1957 [4] made the discovery that interactions with the weak nuclear force lead to parity violation. This discovery had several further consequences such as the discovery of interesting characteristics of certain particles. Most relevant to this thesis, it lead to the discovery that all SM neutrinos have left-handed helicity, which as previously mentioned in the chirality section is directly equivalent to having left-handed chirality for massless or highly relativistic particles. Thus all neutrinos are left-handed and all anti neutrinos are right-handed. This was discovered through an experiment which cleverly utilised beta decays involving electron capture, through a process which can be described as:

$$e(\frac{1}{2}) + A(0) \rightarrow B^*(1) + \nu(\frac{1}{2}) \rightarrow B(0) + \gamma(1) + \nu(\frac{1}{2}) \tag{10}$$

Where the spin is presented in the brackets, A is the nucleus particle, B^* is the daughter nucleus in an exited state, and B is the daughter nucleus in a stable state. Through this process one can measure the momentum and direction of the neutrino, as it must be equal and opposite to the recoil of B^*, and through the conservation of angular momentum, we can also deduce that the spin of B^* must have the opposite sign of the spin of the neutrino. Thus when B^* decays to B by a γ-ray in the opposite direction from the neutrino, the resulting γ-ray will have the same helicity as the neutrino, which can then be measured from the polarisation of the γ-ray.

Neutrino oscillations

Neutrino oscillations were first theorised due to a lack of observable neutrinos in early neutrino detection experiments, where the scientists knew the theoretical amount of neutrinos that should be coming to earth from the sun, and atmosphere, as well as the efficiency of their detectors. Thus they had good estimates of how many neutrinos they should be detecting, however the number of neutrinos they detected were far smaller than the theoretical amount [5][6][7]. This problem can be solved by introducing the possibility of oscillations of neutrino flavours. For these oscillations to occur, the active (interacting) neutrinos are written as a superposition of different neutrino mass eigenstates:

$$\nu_\alpha = \sum_{i=1,2,3} U_{\alpha i}^* \nu_i, \quad \alpha = e, \mu, \tau \tag{11}$$

here U denotes the Pontecorvo-Maki-Nakagawa-Sakata (PMNS) matrix which relates flavor and mass eigenstates of the neutrinos

$$U = \begin{pmatrix} U_{e1} & U_{e2} & U_{e3} \\ U_{\mu 1} & U_{\mu 2} & U_{\mu 3} \\ U_{\tau 1} & U_{\tau 2} & U_{\tau 3} \end{pmatrix} \tag{12}$$

with a common parameterization as given in [8]

$$U = \begin{pmatrix} c_{12}c_{13} & s_{12}c_{13} & s_{13}e^{i\partial} \\ -s_{12}c_{23} - c_{12}s_{23}s_{13}e^{i\partial} & c_{12}c_{23} - s_{12}s_{23}s_{13}e^{i\partial} & s_{23}c_{13} \\ s_{12}s_{23} - c_{12}c_{23}s_{13}e^{i\partial} & -c_{12}s_{23} - s_{12}c_{23}s_{13}e^{i\partial} & c_{23}c_{13} \end{pmatrix} \\ \times diag(i, e^{\alpha_{21}/2}, e^{\alpha_{31}/2}) \tag{13}$$

where c_{ij} is short for $cos(\theta_{ij})$ and s_{ij} is short for $sin(\theta_{ij})$ with $\theta_{ij} = [0, \frac{0}{2\pi}]$ and $\partial = [0, 2\pi]$ and α_{21}, α_{31} are CP violating phases. Treating neutrinos as oscillating superpositions of mass eigenstates lets us explain the disappearances and appearances for a certain flavour of neutrinos that have been observed in experiments. According to the most recent measurements all of the matrix elements are between 0.1 and 0.9, the CP violating phases have not yet been measured directly, but vague estimates can be obtained by fits using the other measurements. So far it has been established that there are at least three separate mass eigenstates all of which have to be different and very small

$$m_i \neq m_j, \forall i \neq j, \quad \Sigma m_i \leq 1eV \tag{14}$$

for $i, j = 1, 2, 3$. With three neutrinos, we get two different mass splittings given by $m_{ij}^2 = (m_i^2 - m_j^2)$. Conventionally ν_1 is taken to be the lower mass in the 1,2 mass splitting, ν_2 is the higher number in this mass splitting and ν_3 is the remaining value. Current mass measurements of the mass splitting are given in Table 1 and a depiction is in Figure 2. The mass ordering (ν_1, ν_2, ν_3) is called normal neutrino mass hierarchy while the ordering $(\nu_3, \nu_1, \nu_2$ is called reverse neutrino mass hierarchy.

mass splitting	best fit	σ range
$\delta m_{21}^2 [10^{-5} eV^2]$	7.37	6.93-7.96
$\delta m_{31}^2 [10^{-3} eV^2]$	2.56	2.45-2.69

Table 1: The mass splitting between neutrino masses [8]

Neutrinos oscillations demonstrate that neutrinos have mass and the SM is incomplete. Neutrinos are to this day the least understood particles of the SM. This makes any experimental effort in this area exciting and necessary to complete the picture of the subatomic world.

Neutrino minimal SM

Due to the observations of neutrino masses, it is quite clear the SM is not a complete theory. This is further compounded upon by the existence of dark matter, dark energy and the baryon asymmetry of the universe which can not be explained by the SM.

These deficiencies of the SM can be solved by adding three new neutrinos, with masses slightly below the electroweak scale, and this has the exciting implication that it might be possible to observe these Beyond the SM (BSM) phenomena at the LHC. These new neutrinos are referred to as being singlets or sterile as
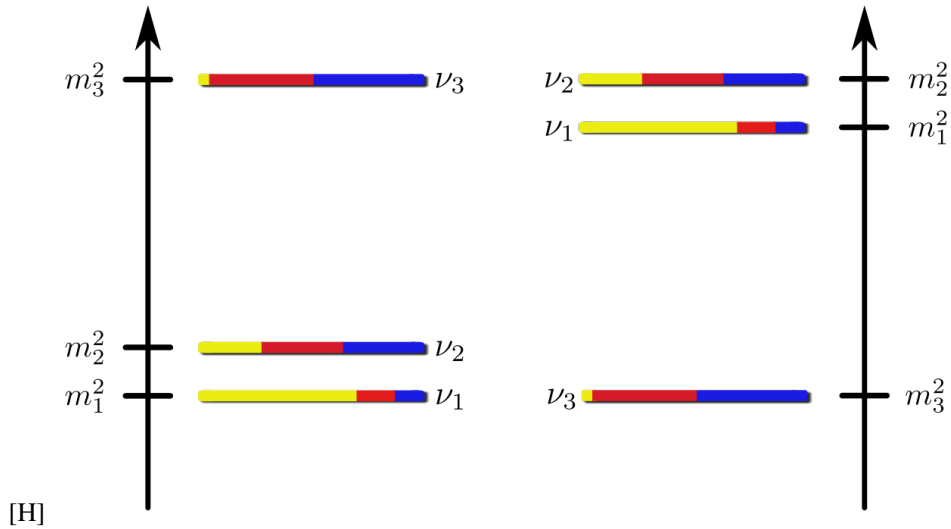
Figure 2: Different possible mass splitting orderings. Colours correspond to the relative flavour eigenstate content: $yellow = \nu_e$, $red = \nu_\mu$, $blue = \nu_\tau$. Figure taken from [9] under creative commons license CC-BY [2].

they don't have either a strong, weak or electromagnetic charge, and therefore don't interact with any of the SM force carrying particles. In order to theoretically describe the existence of neutrino oscillations, it is not sufficient to just generate mass terms for the existing SM neutrinos, we must also explain why masses of the SM neutrinos are as extremely low as they seem to be. This makes it necessary the new neutrinos to have Majorana properties, and allow for a seesaw mechanism in Nature which can explain the low SM active neutrino masses.

A theory including such new particles is called νMSM theory, and it is very popular because it is strongly motivated, provides a clear way to explain neutrino oscillations, the extensions it makes to the SM are very simple and doesn't introduce any new energy scales [10]. Active neutrinos in the SM are described as Weyl particles with no associated mass term, and only a left-handed component interacting weakly with Z and W bosons. By expanding the SM with new right-handed neutrino fields, and assuming neutrinos are Majorana particles, mass terms can be generated without violating any important symmetry. The νMSM particle content is shown in Figure 3.
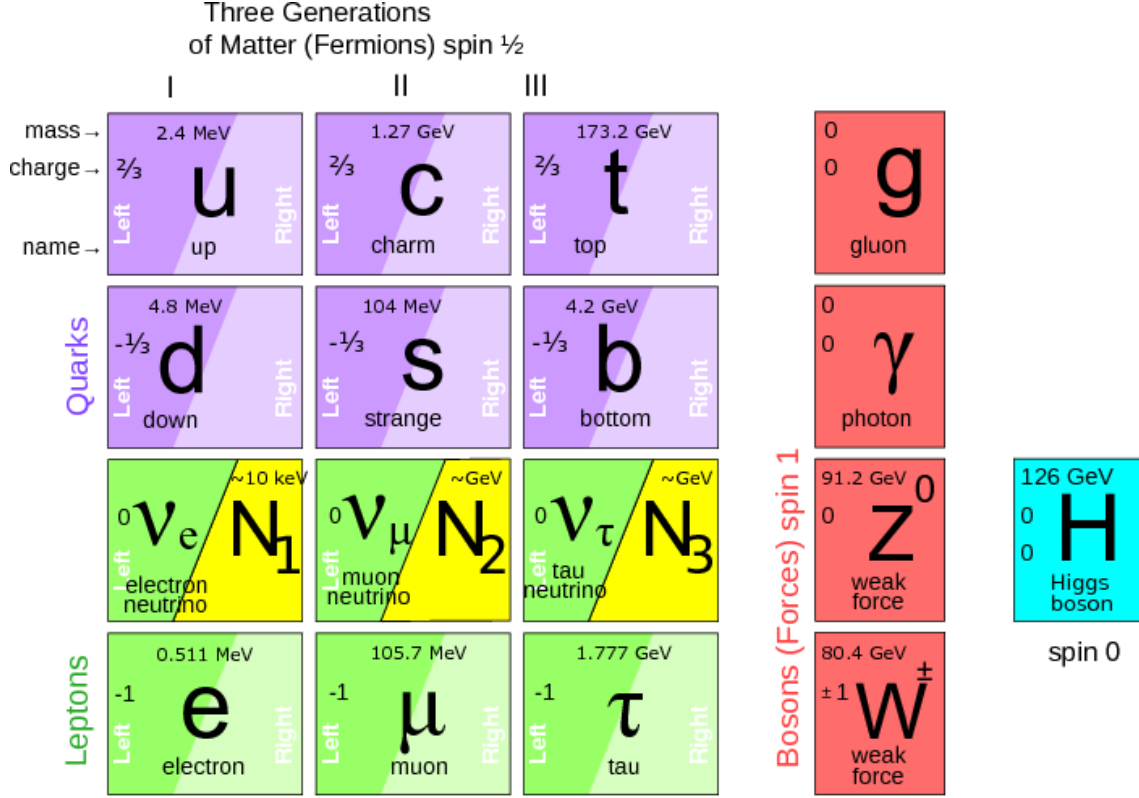
Figure 3: Visualization of the SM of elementary particles with the addition of the three sterile neutrinos from the νMSM. From [11].

Dirac, Majorana and Weyl fermions

In order to explain some of the effects that arise from adding these new right-handed neutrinos to the SM, we first need to go back and look again in greater details at some of the basic properties of the SM. The SM is a relativistic formulation of quantum mechanics. The starting point is the Dirac equation, which is used to describe free fermions with half-integer spin [12]:

$$(i\gamma^\mu \partial_\mu - m)\Psi = 0. \tag{15}$$

Here Einstein notation is used to indicate a sum over the four indices of μ. 's are matrices including spin information. The Dirac equation can be solved to express either a Dirac, Majorana or Weyl field. The most complex of these solutions is the Dirac solution which is unconstrained and takes the form of a four component spinor, whereas both the Majorana and Weyl solutions take much simpler forms. In the case of the Majorana field there is no change under charge conjugations, meaning that Majorana particles are their own antiparticles, and the Weyl field is massless.

In the SM, when interactions are introduced and the Dirac equation is therefore extended, all charged leptons and quarks are represented by Dirac fields, whereas the neutrinos which are considered massless are represented by Weyl fields. There are no Majorana fields present in the SM as the presence of Majorana fields would break the gauge invariance of the equation.

For the remainder of this section the different types of fields will be denoted by different symbols; Dirac fields are denoted as Ψ, Majorana fields as χ and Weyl fields as ψ. The dynamics of fermion fields are described by the Lagrangian density (denoted D from the Dirac equation), which is given as [12]:

$$\mathcal{L}_D = i\bar{\Psi}\gamma^\mu \partial_\mu \Psi - m\bar{\Psi}\Psi. \tag{16}$$

Here the first term represents the kinetic energy density, and the second term represents the potential energy density of the field. m is called the mass of the fermion field, and what it really represents, for quarks and charged leptons - when electroweak forces and the Higgs field are introduced - is the Yukawa interaction of Ψ to the Higgs field divided by the vacuum expectation of the Higgs field itself, as mentioned in Sect.**??**. $\bar{\Psi}$ refers to the Dirac adjoint of the field and is defined as $\bar{\Psi} = \Psi\gamma^0$.

As mentioned, the solutions for the Majorana and Weyl fields are simpler than the Dirac solution. So

first lets look at the properties of Weyl fields. Weyl fermions are massless particles described by a two-component spinor. The Dirac field can be written as the combination of two Weyl fields:

$$\Psi = P_L\Psi + P_R\Psi = \psi_L + \psi_R \tag{17}$$

Where P_L, P_R are the left- and right-handed chiral projection operators, and ψ_L, ψ_R are the left- and right-handed Weyl fields. Expressing the Dirac Lagrangian in terms of Weyl fields we get:

$$\mathcal{L}_D = i\bar{\psi}_L\gamma^\mu\partial_\mu\psi_L + +i\bar{\psi}_R\gamma^\mu\partial_\mu\psi_R - m(\bar{\psi}_R\psi_L + \bar{\psi}_L\psi_R). \tag{18}$$

Here we can see that the Dirac Lagrangian can be written using a single Weyl field to describe a massless Weyl fermion with two degrees of freedom.

In the SM neutrinos are described as two-component Weyl fermions which violate parity invariance (ψ_R non existing, and therefore no mass - interaction with Higgs field - term) but preserve Lorentz invariance [12]. If we introduce a right-handed neutrino field to the, we get a Lagrangian which is split into two parts, where one part within the SM and the other is beyond the SM (BSM):

$$\mathcal{L}_{\nu-SM} = i\bar{\psi}_L\gamma^\mu\partial_\mu\psi_L \tag{19}$$

$$\mathcal{L}_{\nu-BSM} = i\bar{\psi}_R\gamma^\mu\partial_\mu\psi_R - m(\bar{\psi}_R\psi_L + \bar{\psi}_L\psi_R) \tag{20}$$

Here we can see that the mass field is only generated through the Yukawa coupling if there is a right-handed field. Here we can see that $\mathcal{L}_{\nu-SM} + \mathcal{L}_{\nu-BSM} = \mathcal{L}_D$. From this it is however not possible to explain why the neutrino mass is less than 1 eV while the second lightest fermion the electron has a mass of 511 KeV, in order to explain this extremely small SM mass, we need to introduce Majorana properties for the right-handed neutrinos. This is allowed since the right-handed neutrinos transform as singlets when the SM gauge transformation is applied (they don't interact via any of the forces), meaning that any term which only includes the right-handed neutrinos can be added to the SM without breaking its gauge invariance.

Majorana fermions are defined as being invariant under charge conjugation meaning that $\chi^C = \chi$. It means that there is a relation between left and right-handed components. The Majorana mass term of the Lagrangian can be written as:

$$\mathcal{L}_{\nu-BSM} = -\frac{1}{2}m_R(\bar{\chi^C}\chi + \bar{\chi}\chi^C) \tag{21}$$

Adding these right-handed neutrinos to SM forming the νMSM adds three BSM components to the SM Lagrangian in the form of: A Dirac mass term using the Yukawa interaction between the active SM neutrinos and the new sterile BSM neutrinos; a Majorana mass term for the BSM sterile right-handed neutrinos; and a kinematic term for the BSM sterile right-handed neutrinos.

Seesaw mechanism

In a previous section it was shown how we can introduce a mass term for neutrinos by introducing a right-handed neutrino field. In this section we will look at a more general form of the BSM of the relevant Lagrangian. when introducing $\mathcal{N}$ new right-handed neutrinos, the Lagrangian takes the form [10]:

$$\mathcal{L} = \mathcal{L}_{SM} + i\bar{N}_I\partial_\mu\gamma^\mu N_I - (\lambda_{\alpha I}\bar{L}_\alpha N_I\tilde{H} - \frac{M_I}{2}\bar{N}_I^C N_I + h.c) \tag{22}$$

where N_I is the right-handed neutrino singlet field.
I is the index over the number of right-handed neutrinos.
L_α is the leptonic SU(2) doublet.
α index denoting the leptonic generations e, μ, τ
$\lambda_{\alpha I}$ is the Yukawa coupling between the active neutrino of generation α and the sterile neutrino of generation I.
H is the Higgs field represented by a SU(2) doublet.
M_I is the mass of the I'th sterile neutrino.
and lastly h.c. is short for hermitian conjugate.

Because of the non-zero expectation value of the Higgs boson, the Dirac masses M_D are defined by the Yukawa coupling and $\langle H \rangle$. In the νMSM case where we add three right-handed neutrinos to the SM, a 6×6 matrix is present in the Lagrangian. This matrix represents 3 masses for the active SM neutrinos and 3 masses for the new sterile neutrinos. The mass term arising from eq. 22 can be written as [13]:

$$-\frac{1}{2}(\bar{\nu_L} \bar{\nu_R^C}) \begin{pmatrix} 0 & M_D^T \\ M_D & M \end{pmatrix} \begin{pmatrix} \nu_L^C \\ \nu_R \end{pmatrix} + h.c. \tag{23}$$

Here M_D is a 3×3 matrix of the Dirac masses, M is a 3×3 matrix of the Majorana masses for the right-handed neutrinos. The physical state of the system can be found by diagonalizing the mass matrix. In the limit where $M_I >> M_D$ the see-saw mechanism gives rise to 3 almost entirely right-handed neutrinos with large Majorana masses [14]

$$m_{N_I}^{RH} = M_I \tag{24}$$

And 3 almost entirely left-handed neutrinos with very small Majorana masses

$$m_\nu^{LH} = M_D^T M^{-1} M_D \tag{25}$$

Here we see that the SM neutrino masses are suppressed by a factor of M^{-1} which would explain why they are so small. In order to explain the smallness of the SM neutrino masses through the see-saw mechanism, and account for neutrino oscillations, only two heavy right-handed neutrinos are required. However if we also wish to explain the existence of dark matter we need to introduce a third. Additionally adding three sterile neutrinos also follows the general symmetry of quarks and leptons in the SM where quarks and leptons have an opposite-handed counterpart. The addition of these three new sterile neutrinos gives rise to 18 new free parameters, in the form of: 3 Majorana masses, 3 Dirac masses, 6 mixing angles, between active and sterile neutrinos and 6 cp-violating phases.

Parameters of the νMSM

The 18 new free parameters added by the νMSM are tuned so as to explain all the unexplained BSM phenomena. This means that the model is required to be able offer a dark matter candidate as well as explain the observed baryon asymmetry of the universe. The observed rate of neutrino oscillations also provide limits for the mixing angles for the SM neutrinos.

It is shown [10] that the νMSM would in fact be capable of explaining all these BSM phenomena. In this section we will look at the constraints which are relevant to this analysis.

One of the requirements of the νMSM is that it needs to provide a dark matter candidate, this is done through there being three sterile neutrinos labeled N_1, N_2 and N_3, with N_2 and N_3 having a very large masses which are roughly degenerate and a sizable mixing angle with the SM neutrinos. N_1 however would have a much smaller mass and a very small mixing angle with the SM neutrinos, giving it an extremely long theoretical lifetime which would exceed 10^{24}s which is several orders of magnitude longer than the age of the universe, thus making N_1 an ideal dark matter candidate. Due to the extremely low mixing of N_1 with the SM neutrinos, it will however not be relevant to this analysis, which will instead focus entirely on N_2 and N_3.

The requirement of explaining the baryon asymmetry of the universe puts limits on the masses of N_2 and N_3, limiting their masses to the range 150 MeV < $M_{1,2}$ < 100 GeV. Additionally they are limited to having a lifetime below 0.1 s, this limit is required in order to not influence the predictions of the big bang nucleosynthesis.

Sterile neutrinos would only be directly observable through their mixing with SM neutrinos. This makes the potential of discovering them extremely dependant on the strength of the mixing between the sterile and active neutrinos. Mixing between sterile and active neutrinos is characterised by a coupling strength denoted by $V_{\alpha,I}$ (sometimes denoted also by $U_{\alpha,I}$) with α is the index running over the SM lepton generations, and I is the index running over the three generations of sterile neutrinos. The couplings of N_2 and N_3 with the active neutrinos must be identical.

Additionally the coupling is highly dependant on the mass hierarchy of the active neutrinos which is still unknown and pictured in Figure2.

The work in this thesis focuses on a scenario where the coupling between $N_{2,3}$ and ν_μ and ν_τ are non zero. this is a scenario not yet investigated with LHC data. In the νMSM there are three neutrinos, but

depending on how the mass difference $\Delta(M)$ of N_2 and N_3 is small, wrt decay width Γ, or large, then the new physics appears as a Majorana or pseudo-Dirac particle. In both cases the existence of this additional particle manifests itself in Lepton Number Violating (LNV) or Conserving (LNC) processes. In the analysis presented in this work, assuming a good way of identifying or labelling the leptons from W and N decay is found, then the request of same sign (LNV process) or opposite sign (LNC process) electric charge is the easiest handle to determine if there is clear evidence for Majorana nature of a possible new neutrino in the data, or not. In the case an excess is found in the same sign electric charge selection, then it can only be given by a Majorana particle. That will indicate $\Delta(M) >> \Gamma$, although one won't be able to infer information on either the mass difference itself, the or decay width, from such observation. In the case an excess is found in the opposite sign electric charge selection, then it can be given by a Majorana or pseudo-Dirac particle, and by looking at the LNV / LNC ratio, if it is non-trivial, then it would be possible to measure $\Delta(M)$.

Previous experimental tests

There have been several previous searches for N's at different experiments. Target experiments able to test with high intensity the low mass region, setting the strongest limits on mixing in that region. Collider experiments, LEP first and then LHC, probing moderate mixing values for a large area of mass range. The results , pre LHC Run 2, are summarized in Figure 4, for the hypothesis of mixing to μ neutrino flavour only.
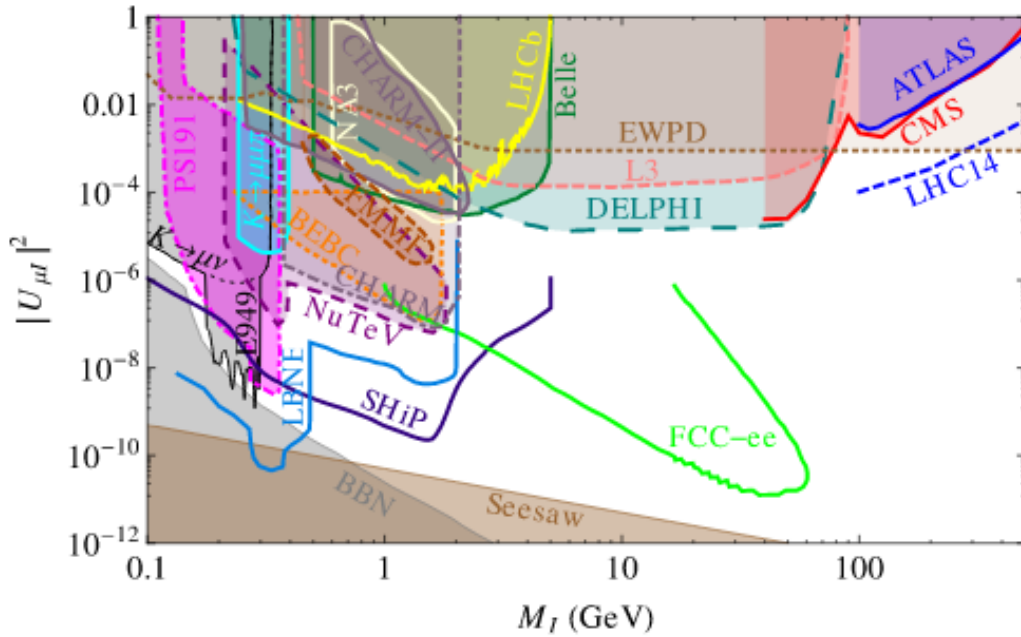

Figure 4: Existing experimental limits $|U\alpha N|^2$ for $\alpha = \mu$ [15]

In 2018 CMS published results [16] for early Run 2, for $35.9\,fb^{-1}$ of proton-proton collisions with a center of mass energy of 13 TeV, and the resulting limits for the muon mixing angle are shown in Figure 5.
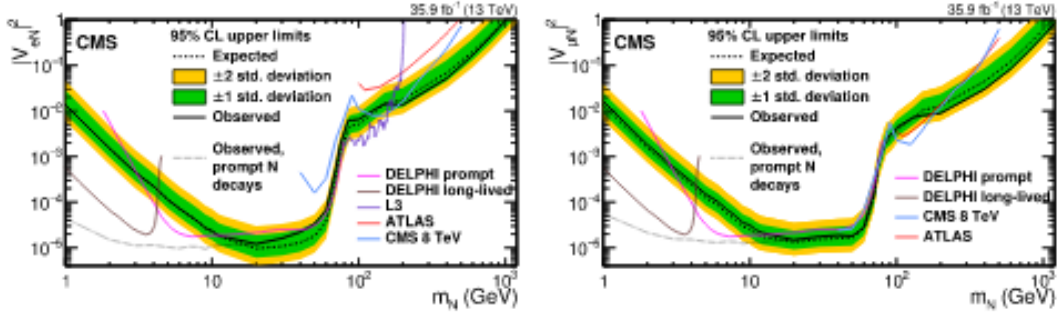
Figure 5: CMS Observed 95% confidence-level exclusion limits for |VαN|² for $\alpha = \mu$ or $\alpha = e$ versus the N mass , obtained in a charged three lepton search [16]. The dotted lines show expected limits and the bands indicate the ranges of expected limits obtained within 1σ and 2σ of the median limit, reflecting uncertainties in signal and background yields.

Additionally a search was done at ATLAS probing for N's in two channels similar to the ones in this thesis, but sensitive to mixing to μ and e neutrino flavor, instead of the taus probed in this thesis. No particle was found, and the resulting limits from this search can be seen in Figure 6.
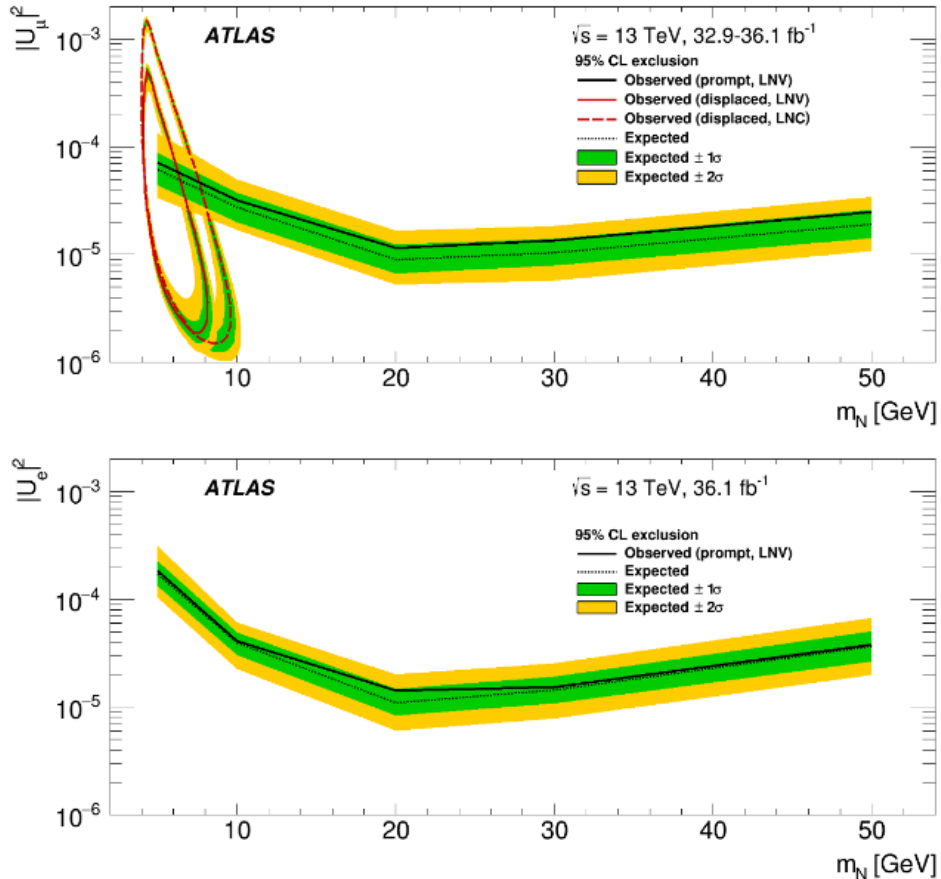

Figure 6: ATLAS Observed 95% confidence-level exclusion $|U_\mu^2|$ (top) $|U_e^2|$ (bottom) versus the N mass for the prompt signature (the region above the black line is excluded) and the displaced signature (the region enclosed by the red line is excluded). The solid lines show limits assuming lepton-number violation (LNV) for 50% of the decays and the long-dashed line shows the limit in the case of lepton-number conservation (LNC). The dotted lines show expected limits and the bands indicate the ranges of expected limits obtained within 1σ and 2σ of the median limit, reflecting uncertainties in signal and background yields. From [17]

The ATLAS Experiment

The ATLAS detector at LHC is a particle detector with cylindrical geometry. It is constructed with multiple circular layers of detectors, each of them ensuring that different particles with varying properties and energies can be measured, in varying properties such as energy, momentum, and trajectory.

The Large Hadron Collider (LHC) is the particle accelerator used by four large experiments, at the European Organisation for Nuclear Research (CERN). It is a multi purpose accelerator, it accelerates protons, lead- and xeon ions, providing the required hadron collisions at the fixed interaction point for each experiment along the ring, namely ATLAS, CMS, LHC-b and ALICE (A Large Ion Collider Experiment).

LHC

The LHC is a circular particle accelerator with a 27 kilometer circumference, used to accelerate hadrons, located to the west of Geneva along the Swiss-French border.

A Figure of the infrastructure for the hadron collisions of the LHC is provided in Figure 7. In order to obtain the proton-proton design center-of-mass collision energy of 13 TeV, protons first go through multiple pre-acceleration steps before the particle-beams enter the main accelerator ring. First protons go through LINAC2 (Linear Accelerator), then Booster (Proton Synchotron Booster), PS (Proton Synchotron) and finally SPS (Super Proton Synchotron) before being injected into the LHC where they reach the final collision energy, which for our search is a center-of-mass energy of 13 TeV.

The beam from the SPS has an energy of 450 GeV and needs to be injected into the LHC, in order to accomplish this the injected beam approaches the LHC beamline from below at an angle of 0.85 mrad [18] there a system called an "injection kicker system" aligns the incoming beam of protons with the existing proton beams in the LHC beam pipe using four fast pulsed magnets. In order for this to work the timing of the SPS accelerator as well as the rise- and fall-times of the injection kicker has to be taken into account.
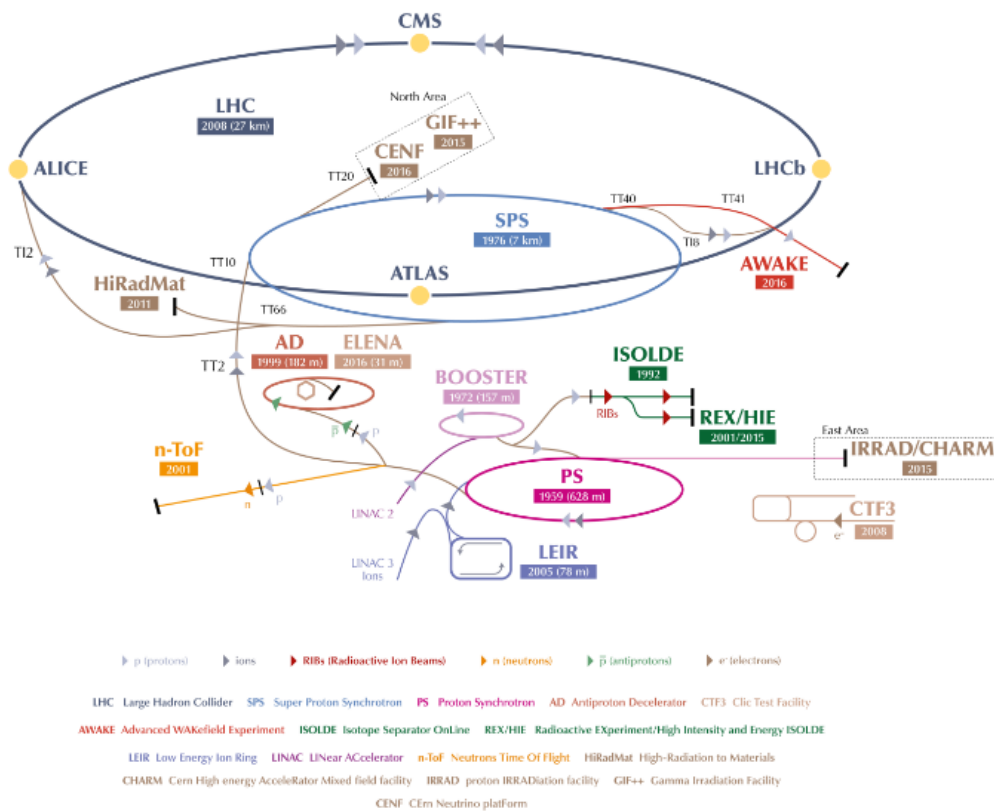

Figure 7: The CERN accelerator complex. The figure shows the different accelerator steps, before the beams enter the LHC, as well as older existing accelerators. Figure from [19]

Inside the LHC accelerator ring there are two beamlines which accelerate protons in opposite directions. The acceleration is carried out by Radio Frequency (RF) cavities; these cavities make sure that protons are

attracted to the next ring segment, while super-cooled powerful electromagnets make sure that the protons stay on the right trajectory within the accelerator. By controlling the magnetic fields with extremely high precision, protons are bunched together in the RF cavities in bundles of about 115 billion protons. The two beamlines are timed such that the particle bundles cross each other in certain interaction points, where they then collide and the results are measured by the experiments.

RF System

As previously mentioned when protons enter LHC they have an energy of about 450 GeV, so in order to obtain the 13 TeV collision energy used in this search the protons have to be further accelerated until they obtain an energy of 6.5 TeV, this is done through the RF (radiofrequency) cavities this energy ramp takes about 20 minutes.

While in the RF system protons experience a force due to the induced electromagnetic field. By using a hollow structure with an oscillating magnetic field and connecting tubes the protons can be accelerated standing wave in the desired direction for each beamline, this makes the protons experience a varying force depending on their energy such that less energetic protons experience a stronger force and vice-verse for the highly energetic ones, this helps with the bunching of the protons, as they will all converge towards the same energy, this bunching is also necessary to increase the likelihood of collisions in each beam crossing. The electromagnetic field in the RF cavities oscillates at a frequency of 400 MHZ. The two beamlines at the LHC has independent RF systems, each containing two cryomodules and four RF cavities, the cavities are made of copper and sputtered with niobium, which is a similar setup to the previous high energy LEP (Large Electron Positron) detector accelerator which was housed in the same tunnel, except at LEP the niobium was applied in the form of sheets instead of sputtering.

Superconducting Electromagnets

In order to keep the particle beams on a path that doesn't have them exit the circular LHC, which they circle eleven thousand times per second, a large amount of lattice magnets are placed around the ring in order to bend the particles trajectories.

Due to the circumference of the ring being relatively small compared to the energy of the particles accelerated within it, extremely strong magnetic fields are needed and therefore superconductive electromagnets are used, these magnets have a magnetic field strength ranging from 6.5 to 8.5 T which requires the magnets to be cooled to temperatures below 2 K. LHC mostly uses dipole magnets (depicted in figure 8, 9) in order to bend the trajectory of particle beams, while quadrupoles are used to focus the particle beams and otherwise tune beam parameters. These supercooled magnets are constructed from NbTi windings.
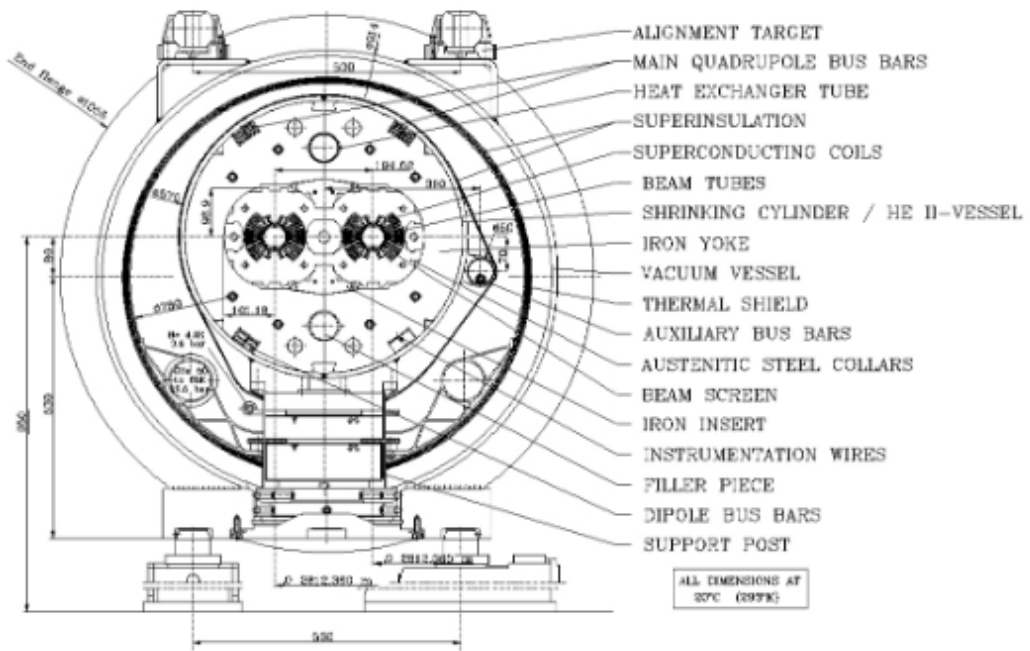
Figure 8: Cross section of the LHC line showing the two beamlines and dipole magnets. From [18]
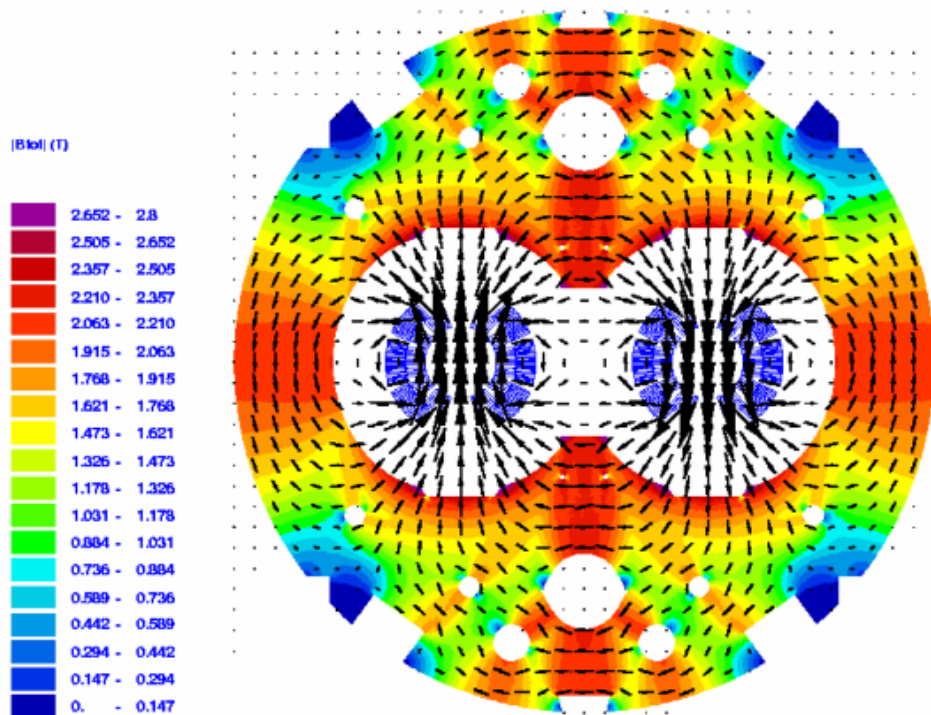

Figure 9: Cross section of the LHC line showing the dipole magnetic flux. From [18]

Cryogenics and vacuum

In order to keep the highly energetic particle beams in a circular trajectory inside the relatively small LHC accelerator extremely strong magnetic fields are required, which in turn means that the magnets maintaining

these magnetic fields needs to be kept at a temperature below 2 K. In order to maintain this low operating temperature LHC uses a cooling system which utilizes two-phase superfluid helium [828526]. LHC uses a quasi-isothermal cooling system where heat is transported from the magnets using a QRL (Cryogenic Distribution Line) situated in the tunnel of the LHC. Refrigerators for the helium and storage vessels for the nitrogen are placed at eight dedicated storage points throughout the LHC ring, the nitrogen is however only used for the precooling of machines and the use of nitrogen is prohibited in the tunnel.

Due to these cooling storage points being strategically placed throughout the 27 kilometer long tunnel, the cooling liquids never need to be transported more than 3.3 kilometers which also serves as a form of redundancy. The RF cavities throughout the ring are enclosed in cryostats where each RF system cools four cavities.

Both the QRL and cryomagnets use an insulation vacuum and operate at roughly 10×10^{-4}Pa, although the vacuum requirements for the beamlines is much higher. Requirements for vacuum strength are expressed as gas densities and compared with hydrogen, the required value for the vacuum requirement of the beamline is stated in [18] as being $10 \times 10^{15} H_2 m^{-3}$ which allows for a beam lifetime in excess of 100 hours, the major limiting factor on this lifetime is nuclear scattering effects of protons on residual gas.
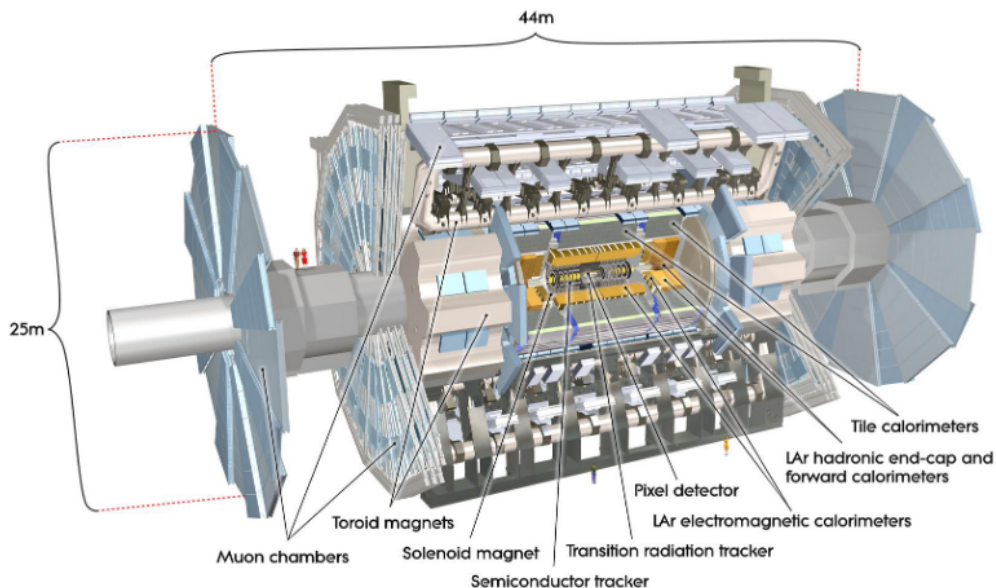
ATLAS subdetectors

Figure 10: Computer generated rendering of the ATLAS detector and its subsystems, including geometry and placement. From [20]

The ATLAS detector shown as a computer rendering in Figure 10., the ATLAS detector consists of Inner Tracking Detector situated closest to the interaction beamline, this is surrounded by a thin superconducting solenoid generating a 2T axial magnetic field, outside that there are the electromagnetic and hadronic calorimeters and finally there is the muon spectrometer which incorporates three large superconducting toroid magnets.

The Inner Tracking Detector consists of three layers which provide charged particle tracking, charge, sign and momentum measurements, but only within the pseudorapidity range $|\eta| < 2.5$, these three layers consist of the three sub-detectors: PIX (a silicon Pixel Detector) which supplies high-granularity measurements of the track, after the first run of the LHC this was expanded with the IBL (Insertable B-Layer) [24,25] the next layer is the SCT (SemiConductor Tracker) on the outside of the SCT is the TRT (Transition Radiation Tracker) which enables radially extended track reconstruction up to $|\eta| = 2.0$ which enhances pattern recognition as well as momentum resolution, additionally it helps to provide particle identification information over a wide range of energies.

The final layer is the calorimeter system which covers a pseudorapidity range of $\eta < 4.9$. Electromagnetic-calorimetry is obtained through high-granularity LAr (lead/liquid-argon) detectors in the pseudorapidity

range $|\eta| < 3.2$, this range is expanded by the forward calorimeter which is also an LAr detector. Hadronic calorimetry is provided by the steel/scintillator-tiles in the region $|\eta| < 1.7$ segmented into three barrels, a central barrel and two extended barrels. The hadronic calorimetry is extended to $|\eta| < 4.9$ with a copper/LAr detector as well as a copper-tungsten/LAr detector.

Coordinate system and common quantities

ATLAS publications generally use the ATLAS coordinate system, which is a three-dimensional cartesian (x,y,z) space defined as having its origins in the proton-proton interaction point, the z direction is defined as being the along the beamline, with the x and y axis forming the plane transverse to the beamline, the x-direction is the axis parallel to the ground with the positive part going toward the center of the LHC, and the y-direction is the vertical direction and the positive axis points upwards. The azimuthal angle is measured around the beam axis and is denoted as Φ, and the polar angle is denoted as θ, this thesis like ATLAS publications makes frequent use of pseudorapidity which is defined as:

$$\eta = -logtan(\frac{\theta}{2}) \tag{26}$$

This converges in the relativistic limit to the common definition of rapidity, as can be seen by writing it as both a function of particle momentum $\vec{p}$ and longitudinal momentum p_L which is the projection of $\vec{p}$ along the beam axis:

$$\eta = \frac{1}{2}log(\frac{|\vec{p}| + p}{\vec{p} - p_L}), \quad y = \frac{1}{2}log(\frac{E + pL}{E - p_L}) \tag{27}$$

for y rapidity. When referring to a transverse variable this will be denoted by a subscript T, such as p_T, where the transverse quantity is a projection on the x/y plane.

Inner detector

The three systems that make up the inner detector are shown in Figure 11. with their respective positions around the interaction point. The inner detector covers the pseudorapidity range $|\eta| < 2.5$ and resolves the impact parameter with a precision of < 15 μm. Additionally the inner detector also offers precise three-dimensional vertexing with a z-axial resolution for the vertex reconstruction of $\sigma(z)$<1mm which enables good b-jet tagging capabilities [21]. The inner detector offers excellent momentum resolution which makes it instrumental in the identification of charged particles.
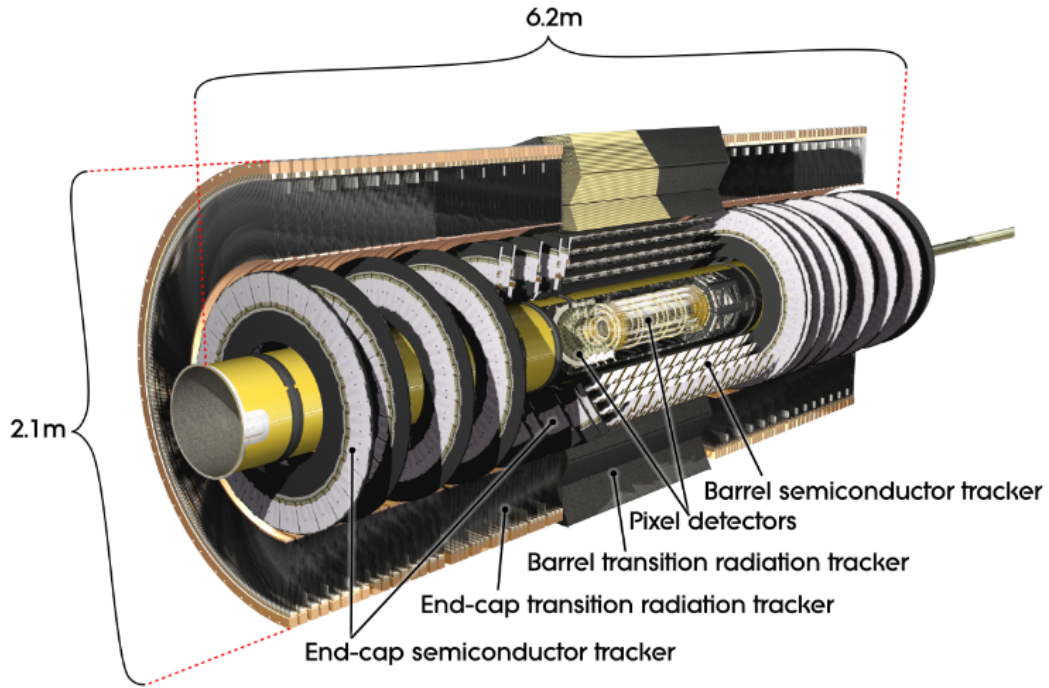
Figure 11: Inner tracker of ATLAS. From [22]

Silicon pixel detector The PIX detector, shown in Figure 12, is the detector nearest to the interaction point, being situated at a radial distance of 50.5 to 194.6 mm from the interaction point and a z-axis distance of 0 to 650 mm.

The detector is composed of silicon pixel sensors which provide high granularity while measuring charged particles which due to the layout of the detector traverse at least three layers for trajectories with $\eta < 2.5$.

PIX consists of three layers of parallel to the beampipe and three pixel rings in the forward- and backwards region called the end-caps.
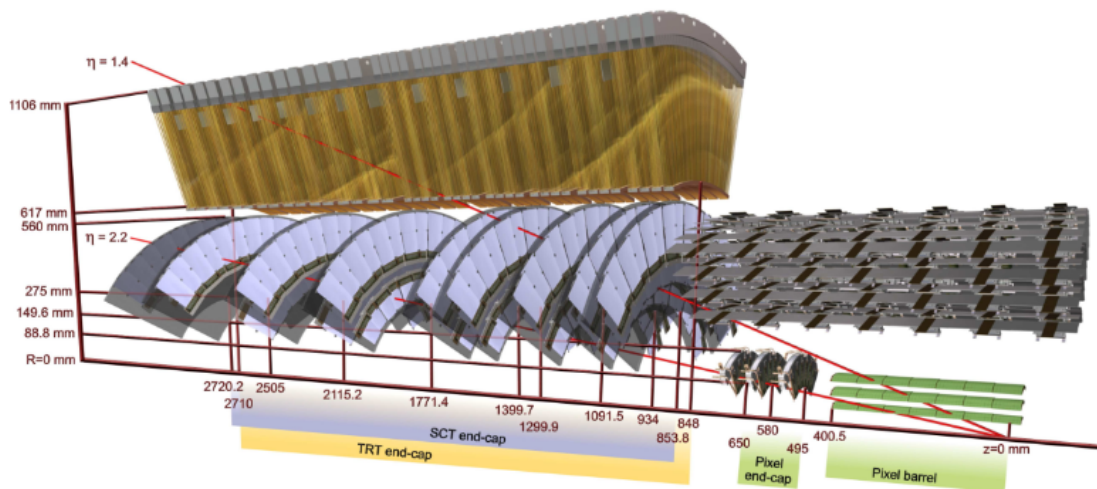

Figure 12: Rendering of PIX sensors being traversed by two charged tracks of 10GeV p in the end-cap with η=1.4, 2.2. From [23]

The semiconductors are 256±3 μm thick oxygenated n-type wafers, they contain n^+ implants on the read-out side and the $p-n$ junction on the back side.

21

Due to the rest of the inner detector being vulnerable to radiation this influenced the design choice especially with respect to operation voltages, the type of semiconductor is changed after $F_{neq} \approx 2 \times 10^{13}$ cm^{-2} (neutron equivalent fluence [24]) as well as increasing the depletion voltage. When this inversion happens the junction will move to the front side [21]. the pixels offer a $50 \times 400 \mu$m^2 detection size.

In addition to the radiation sensitivity the temperature also plays a large part in the noise on the sensor measurements as well as for the aforementioned annealing, therefore the sensors are cooled with a coolant of approximately 25°C down to 5 to 10 °C for operation. The repeated cooling and heating cycles with their corresponding expansion and contraction was taken into account in the planning of the detector.

The alignment tolerance for the pixel sensors is 10 to 20μm for both the radial and axial directions and for the three layers, for the end-cap disks it is 20μm on the radial direction and 100μm in the axial direction. This offers a an accuracy of 10μm in azimuthal direction and are aligned within 7μm.

After the first run of the LHC the beampipe was replaced with a smaller model, which had a 25mm inner radius, where the old one was 29mm, this afforded enough additional space to allow for a new layer pixel layer, namely the aforementioned IBL, which was placed the formerly innermost pixel layer and the beampipe this additional layer provides a big improvement to tracking due to its closer proximity to the interaction point.

The tilted alignment of the IBL is shown in Figure 13. and provides a near complete coverage in azimuthal angle.
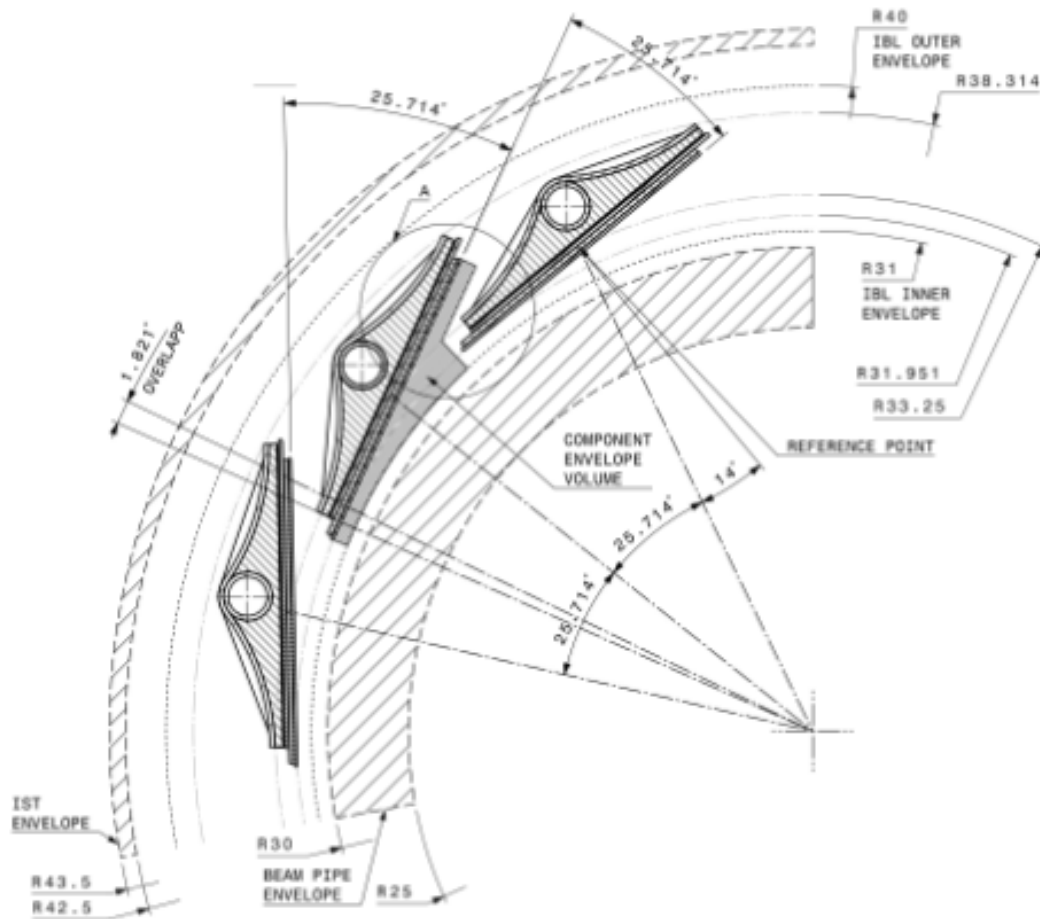
Figure 13: IBL alignment of pixel sensors: rϕ view. From [25]

Silicon microstrip tracker The SCT consists of single sided p-n silicon sensor [26], it supplies four barrel layers ($|\eta| < 1.1 to 1.4$), while the the sensors initially operate at 150V the operation voltage needs to be increased to between 250 and 350V due to strong radiation. The sensors are 285±15μm thick thus making them thicker than the PIX sensors, they balance cost efficiency and operationability in terms of voltage and reliability.

The SCT works as an extension of PIX and is positioned 299 to 560mm radially from the interaction point,

and expands to 2720.2mm in the z-axis for the discs and 749mm for the barrel.

Each module consists of two times 768 active strips, where a strip a strip consists of two daisy-chained 6cm long sensors, the strip pitch is optimized for resolution to $80\mu m$.

Like PIX the SCT was designed to work at low temperatures and is therefore also connected to the inner detector cryostat.

Transition radiation tracker Even though the TRT is designed to run at room temperature, it is still connected to the inner tracker cryostat, it is situated at 563 to 1066mm radially from the interaction point, and axially in the z-direction it extends from 712mm for the barrel, and 2710 mm for the end-cap.

The detector consists of drift tubes with a diameter of 4 mm, inside of which a mixture of 70 % Xe, 27 % CO_2 and 3% O_2 mixture is flushed with 5 to 10 mbar over-pressure. The drift tubes form three rings in the barrel section and two sets of wheels in the end-cap. The first set of wheels in the end-cap consists of 12 wheels and the second set consists of eight, in both sets a wheel consists of 8 successive drift tube layers, the set furthest from the interaction point uses a larger spacing between the layers.

During the second run of the LHC only the third ring of the barrel used the gas mentioned above while the first two layers where flushed with an Ar/CO_2 mixture. In 2018 the O_2 content of the mixture was lowered to 1.5% in order to avoid sparks.

The anode wire is made from tungsten, has a diameter of $31\mu m$ and extends 71.2 cm in either direction from the interaction point. At the middle point of the wire it is fastened to the tube wall thus ensuring that the wire sags by less than $15\mu m$, this fastening results in some inefficiency of 2 cm near the center of the anode.

The tubes are read out from either end and operate at -1530 V, obtaining a gain of 2.5×10^4, with an electron collection time of 48 ns.

The TRT end-caps don't extend past $|\eta|$=2. The barrels are interleaved with fibers and the end-caps are interleaved with foils in order to provide transition radiation for the traversal of charged particles.

The xenon gas mixture used in the tubes plays a vital role in allowing the TRT to combine tracking information with additional particle identification based on transition radiation photon detection, this is possible because the gas mixture has low absorption of photons in the energy range relevant to the transition radiation, this attribute allows for discrimination between hits in the inner detector which could be caused by either electrons or pions, by looking at the fraction of high-threshold hits on the track, in order to do this the TRT outputs an extra bit for any signal which passes a specified threshold at any point within a 25 ns window.

Since transition radiation relies on the relativistic γ factor, and electrons have a higher γ factor than pions, electrons have a higher probability of emitting transition radiation photons, The opening angle between the original electron tracks and the tracks of their transition radiation photons are highly colinear and therefore translates the amount of high-threshold hits to a property of the charged particles going through it. At ATLAS a likelihood-based identification is then applied to distinguish between pions and electrons.

Electromagnetic calorimeters

The EM calorimeter is separated into the barrel which covers $|\eta|$<1.475 and the end-caps which cover 1.375<$|eta|$<3.2, which means that it covers the full azimuthal angle Φ up to $|\eta|$<3.2.

It is designed to measure electrons, protons, jets and E_T^{miss} with good precision and provide good trigger information.

The EM calorimeter consists of is made up from three absorbers with gaps in between them, these absorbers are laid out in an accordion shape, these absorbers are made out of lead with a thickness of 1.53 mm for $|\eta|$<0.8 and 1.13 mm outside of it, this shape naturally the complete Φ coverage. In between the absorbtion layers conductive copper Readout electrodes are placed, there are three total layers of copper where the two outer ones form the high voltage potential, and the inner one reads out the signal. The EM calorimeter uses LAr as the active medium.

The three independent readout layers exhibit different granularity with respect to the η direction, these layers are shown i Figure 14. the granularity gets courser when progressing through the successive layers, most of the energy is absorbed in the second layer, which leaves only the tail of the electromagnetic showers.
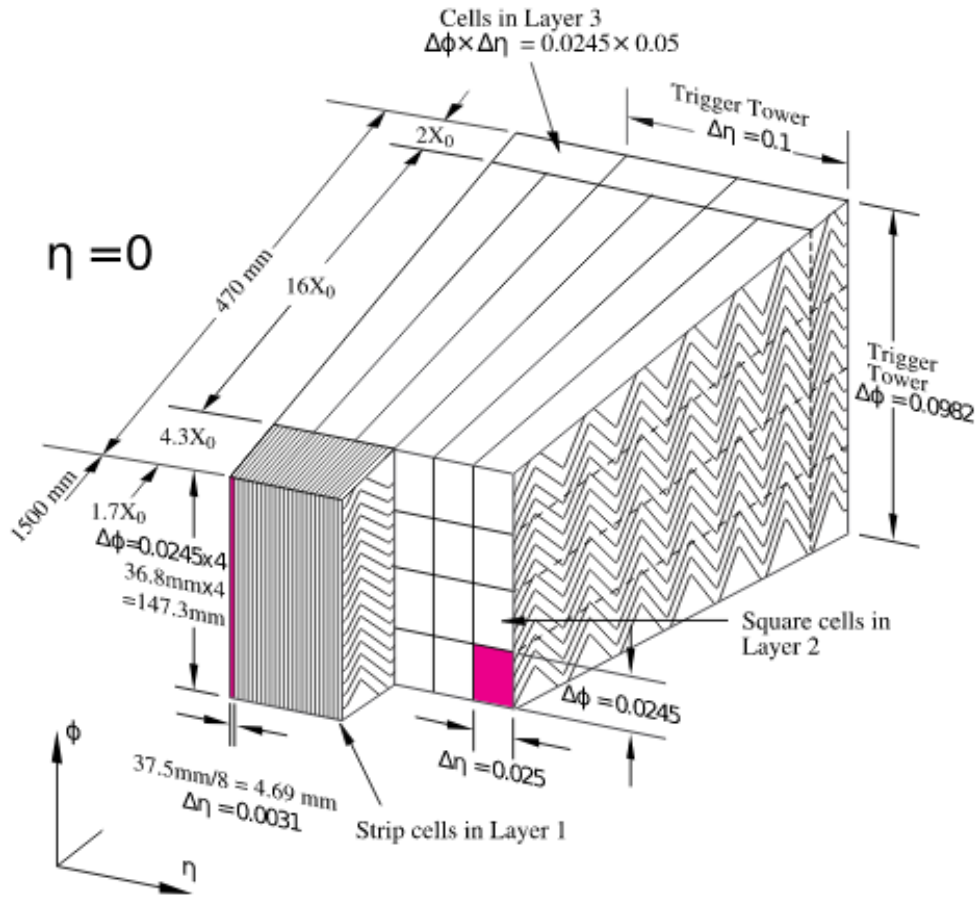
Figure 14: Example of EM calorimeter barrel module layout, From [27]

Each of the three components (barrel and two end-caps) are housed in individual cryostats, whereas the EM calorimeter and solenoid magnet after the inner detector share a vacuum vessel, which saves on material by limiting the amount of vacuum walls needed.

Hadronic Calorimeters

In order to optimise particle identification ATLAS has three different hadronic calorimeters namely: a tile calorimeter, HEC (LAr End-cap calorimeter) and FCal (LAr forward calorimeter).

Tile calorimeter The tile calorimeter [28] consists of a barrel and two extended barrel parts, it uses steel for the absorbers and scintillation panels for the active material.

Between the central barrel and the extended parts there is a 600 mm gap which contains the cabling for the inner detector, as well as the LAr cables, and supply electronics, the gap also contains calorimeters and scintillators in order to recover some of the energy which would otherwise be lost in these regions.

The main barrel covers $|\eta|<1$ while the extended barrels cover $0.8<|\eta|<1.7$ [29].

The primary purpose of the tile calorimeter is to provide additional information for the energy reconstruction of jets produced in pp collisions along with measuring missing transverse momentum (p_T^{miss}).

It consists of 64 modules as shown in Figure 15a. each module consists of both scintillators and steel, each layer consists of a 5 mm thick master plate, with 4 mm thick spacer plates on top, these are assembled in a staggered fashion in order to make room for the scintillators. The light emitted by the scintillators is collected at the edges of the tiles using two wavelength-shifting fibers, which are Photomultiplier tubes at the top of each module.

(a) Schematic of tile calorimeter module. Figure from [36].
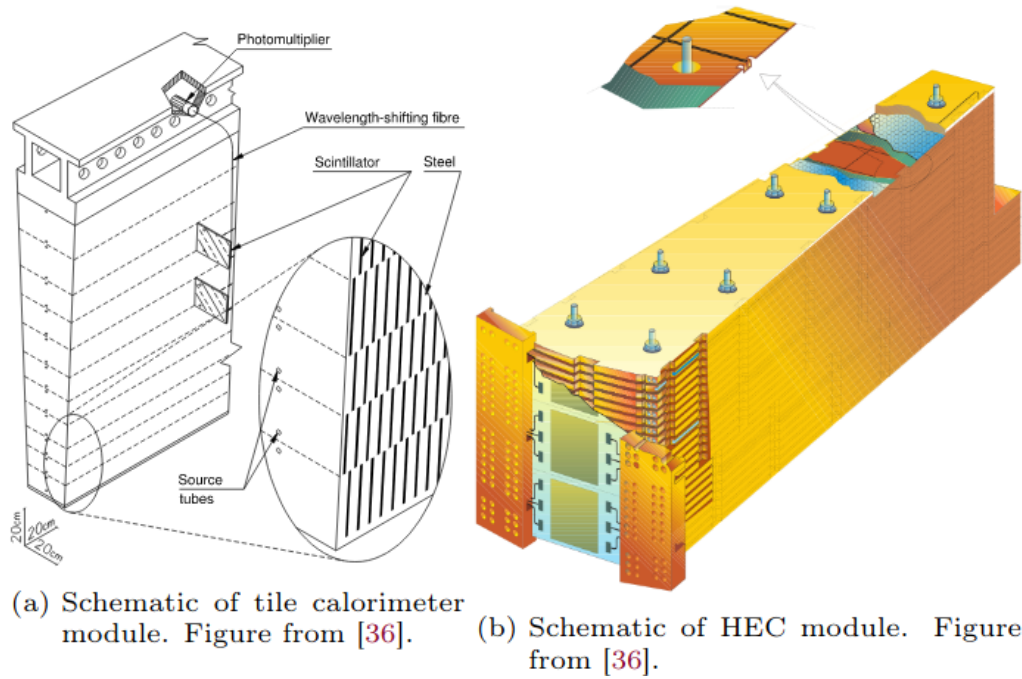
(b) Schematic of HEC module. Figure from [36].

Figure 15: Selection of hadronic calorimeter modules, From [23]

The radial depth of a module is roughly 7.4 interaction lengths and each module offers a $\delta\Phi \times \delta\eta$ resolution of about 0.1×0.1.

Hadronic end-cap calorimeter The HEC [Fabian 58] covers the $1.5<|\eta|<3.2$, it consists of two wheels called the front- and rear-wheels, both wheels have a radius of 2.03 m and consist of copper plates with 8.5 mm gaps and use LAr as the active medium.

The front-wheel consists of 24 copper plates of 25 mm thickness while the rear-wheel consists of 16 copper plates of 50 mm thickness, in the gaps between the copper plates three parallel electrodes are placed in a similar manner to the EM-calorimeter in which the two outer electrodes have a high voltage applied whereas the middle one is used for readout. Both wheels consist of identical modules see (Figure 15b). These modules are wedge shaped and fixed to a central ring as well as the periphery fixture. The HEC supplies a $\delta\Phi \times \delta\eta$ resolution of 0.1×0.1 for the front wheel and 0.2×0.2 for the rear-wheel.

Forward calorimeter The forward calorimeter covers the $|\eta|$ range between 3.1 and 4.9. Since the FCal is only 4.9 m from the beamline it experiences a large particle flux, this fact had a large influence of the design choices for the detector, for example the gaps in the FCal are kept small in order to avoid ion build-up issues.

The FCal is made up of small-diameter rods situated inside tubes which run parallel to the beamline [30], there are three 45 cm deep FCal modules, enumerated from 1-3 based on their distance from the interaction point, with the closest being 1 and the furthest being 3. FCal 1 uses copper as its absorber material whereas FCal 2 and 3 uses tungsten in order to provide stronger containment of particles.

Following the final FCal module there is a brass shield in place in order to reduce background, and protect the end-cap muon system from radiation damage.

FCal 1 consists of copper plates stacked behind each other, these plates have a total of 12260 holes drilled through them parallel to the beamline, each of these holes are filled with electrode systems which consist of co-axial copper rod, as shown in Figure 16a. the LAr is placed around these rods and between the copper plates.

For FCal 2 and 3 two copper endplates with a thickness of 2.35 cm are filled with tungsten slugs, the rods spanned between them are similar to the ones in FCal 1 but with tungsten instead of copper.
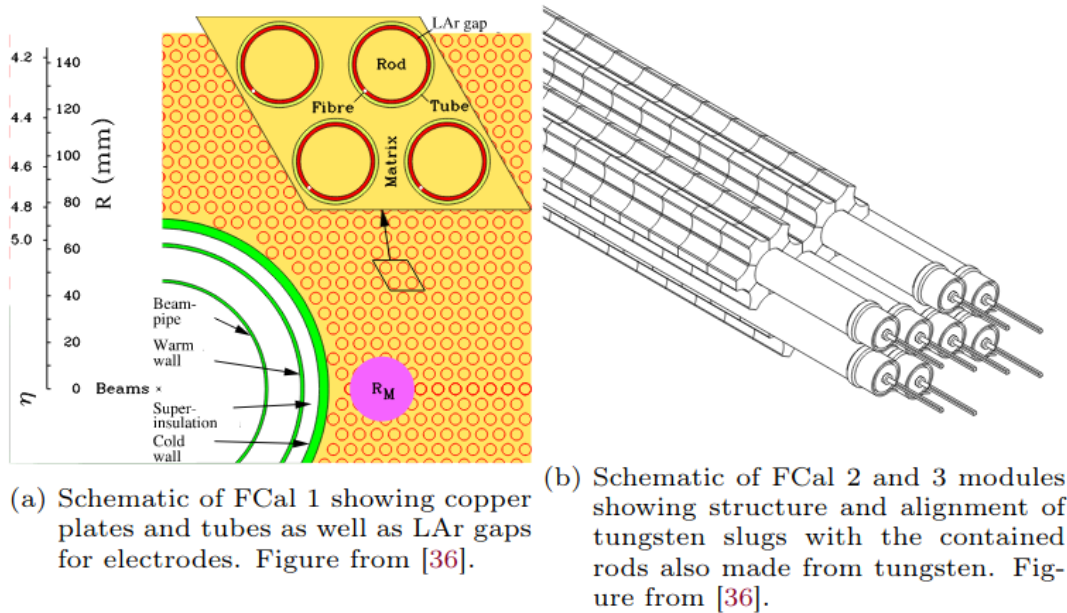
(a) Schematic of FCal 1 showing copper plates and tubes as well as LAr gaps for electrodes. Figure from [36].

(b) Schematic of FCal 2 and 3 modules showing structure and alignment of tungsten slugs with the contained rods also made from tungsten. Figure from [36].

Figure 16: Schematics of FCal modules, From [23]

Solenoid and toroid magnets

In order to measure the momentum of charged particles strong magnetic fields are needed in order to bend the trajectories of even very high energy particles to an observable degree while they are traversing the ATLAS detector.

In order to do this the ATLAS detector uses four different magnet systems which store a combined 1.6 GJ. These systems consist of a central Solenoid magnet situated just after the inner detector, along with a central and two end-cap toroid magnets.

Solenoid magnets In order to both fulfill the requirement for the inner detector to have a strong magnetic field as well as save on material in the limited space in front of the calorimeters, a single layer coil was installed just outside of the inner detector.

The extra material that this coil makes up corresponds to 0.66 radiation lengths and the solenoid magnet [23],[31] measures at a stored-energy-to-mass ratio of 7.4 kJ kg^{-1}, This results in an axial magnetic field at the center of 1.998 T, and uses a nominal operational current of 7730 kA. The solenoid magnet consists of a wound high-strength Al-stabilized NbTi conductor and measures an inner diameter of 2.46 m and an outer diameter of 2.56 m. The solenoid magnet has both a charge and decharge time of 30 minutes.

Toroid magnets The magnetic field for the muon spectrometers and calorimeters is provided by the barrel and end-cap toroid magnets [23], [32] and measures at 0.5 and 1 T respectively. The barrel toroid magnet consists of eight coils which are encased in stainless steel vacuum containers, each with a lengths of 25.3 m. The diameter of the inner toroid magnets is 9.4 m and the outer toroid magnets is 20.1 m, like the solenoid magnet, the toroid magnets consist of windings, which are made of Al-stabilized Nb/Ti/Cu conductors.

Due to the large size of the toroid magnets a large cooldown time is needed, which for 4.6K is given by five weeks.
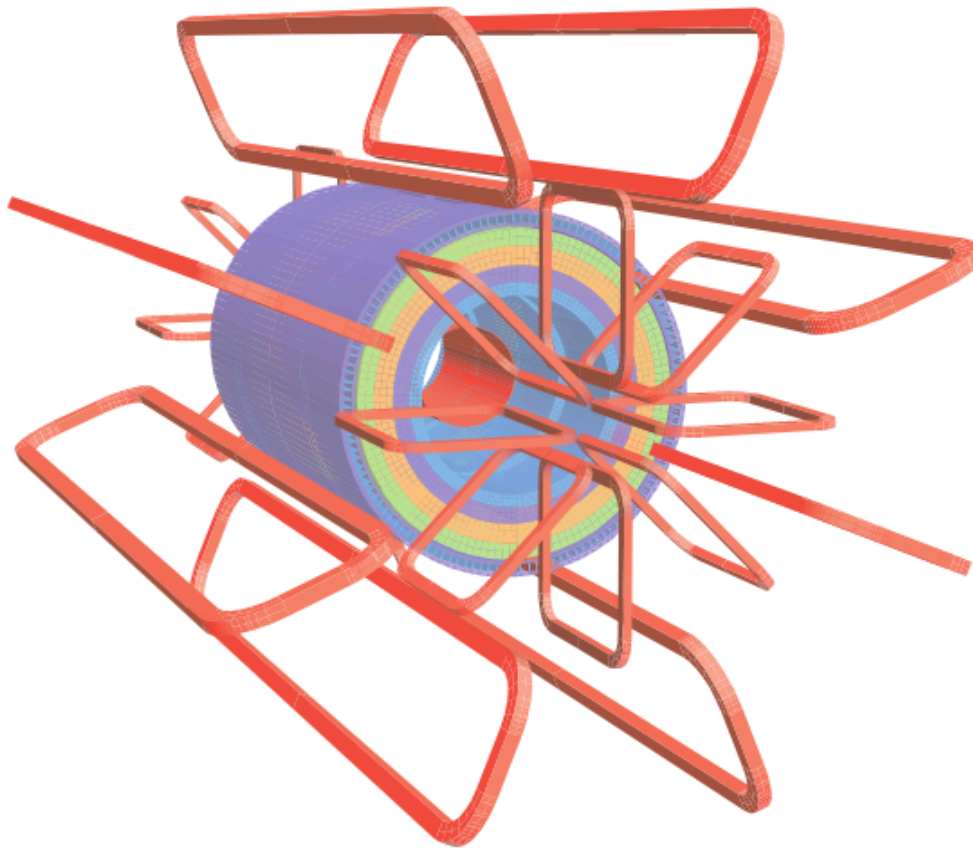
Figure 17: Schematic of the ATLAS magnet windings and tile calorimeter steel, the solenoid windings are depicted inside the calorimeter volume, From [23]

Muon spectrometers

The muon spectrometer form the outside part of the ATLAS detector, since muons are the only particles which are not stopped by the ATLAS calorimeters, this offers an excellent opportunity to between muons and other particles, this also means that the environment in the muon spectrometers is almost free from all other particles produced in the interaction point. The muon spectrometer is generally designed to detect all charged particles, in the range $|\eta|$<2.7 which make it all the way through the ATLAS detector and measure their momentum. Since high energy particles don't experience a high degree of trajectory bending from the magnetic fields of ATLAS large spacing and and distances are needed to get good precision on momentum measurements. The muon spectrometer offers good resolution for particles with energies between 3 and 3000 GeV and ensures a 10% p_T resolution for 1 TeV particles.

The muon spectrometer consists of three cylindrical shells around the z-axis with radii of 5, 7.5 and 10 m in the barrel region, while in the end-cap region it consists of four wheels, at a z-distance of 7.4, 10.8, 14 and 21.5 m from the interaction point. Parts of the muon spectrometer have a gap at $|\eta| \approx$0 in order to enable service lines for other detector parts.

All of the detectors in the muon spectrometer except the first wheel of the end-cap is made up of MDT, whereas the first wheel of the end-cap sections are made of a Cathode-Strip-Chamber (CSC) which is capable of withstanding a higher counting rate.

The full muon spectrometer offers a resolution of 40 μm in the bending plane and a resolution of 5 mm in the transverse plane due to differences in the readout.

An important point for the design choices in the muon spectrometer, is the required sagitta resolution for the p_T resolution: namely that along a 500 μm stretch in the z-axis a resolution of $\leq$50 μm. This is achieved by knowing the position of strips and wires in the CSC and MDT to 30 μm resolution and requires a high-precision optical alignment system which constantly monitors the position and internal deformations, on top of those systems track-based alignment algorithms are used for cross-checks.
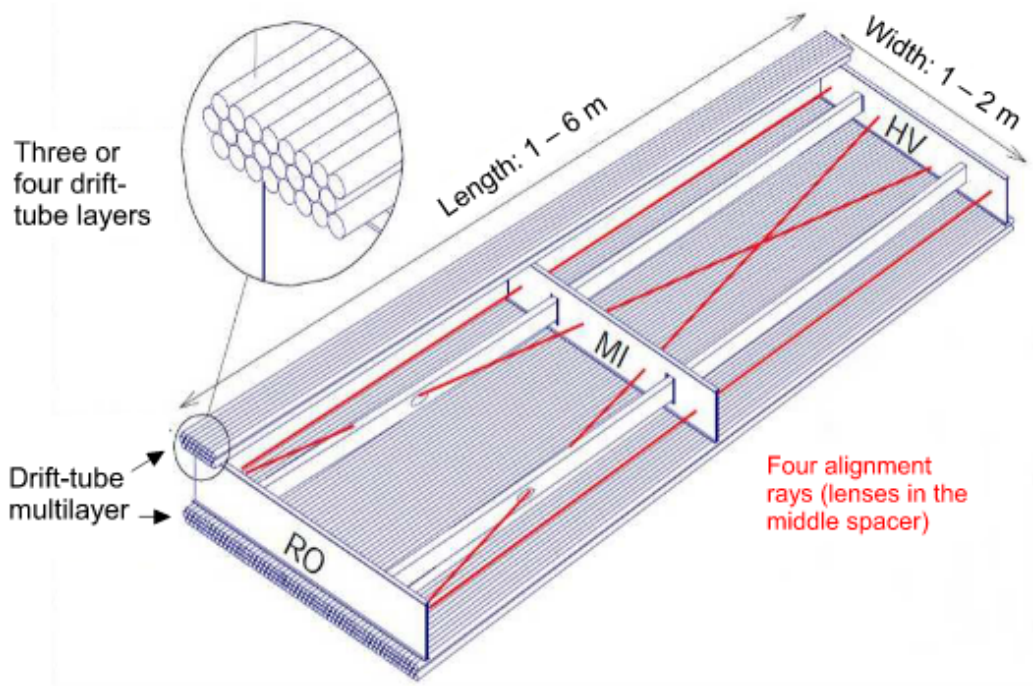
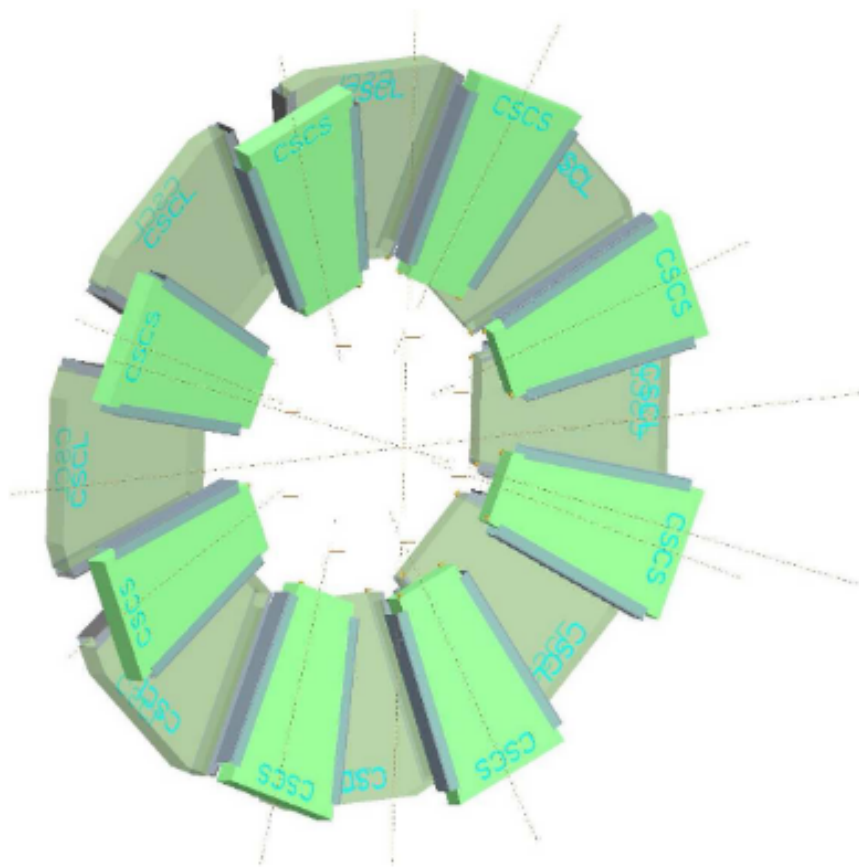Figure 18: Schematic of muon spectrometer Monitored Drift Tube Chambers (MDTs), From [23]

Figure 19: Schematic of muon spectrometer CSCs, From [23]

Each MDT consists of between three and eight layers of drift tubes filled with Ar/CO$_2$ gas in a 93/7

ratio at a pressure of 3 bar. The central anode wire of the drift tubes is made of tungsten-rhenium with a diameter of 50 μm, all of the drift tubes are operated at a potential of 3080 V. The drift tubes have a long drift time of 700 ns, this long drift time necessitates a separate triggering detector, and has a resolution of charged particles of 80μm. In total the MDTs can obtain a resolution of 35 μm by using the combination of the different layered tubes.

In the forward region with $2<|\eta|<2.7$ the first wheel is using CSC as they offer a better rate capability, while MDTs can handle a rate of 150 Hz cm^{-2} CSCs can handle all the way up to 1000 Hz cm^{-2} which is needed in the end-cap regions, the other three wheels in the end-cap regions however use MDTs.

The end-cap muon spectrometer only covers the range $|\eta|<2.7$, which is sufficient within the rate limitations of the MDTs.

The CSCs also offer a better time resolution. They are multiwire proportional chambers with cathode planes which are arranged in two discs with eight chambers each, as seen in Figure 19. The wires are installed in the radial direction but are parallel in each chamber with the central (radial) wire, the cathode and anode wire-wire spacing is equidistant and a gas mixture of Ar/CO$_2$ in a 80/20 ratio is used. The operation voltage used is 1900 V and a resolution of 60 μm is achieved.

Because the readout of both the MDTs and CSCs is quite slow and one of the goals of the muon spectrometer is to trigger on muons, additional fast triggering chambers are required in order to trigger on muon tracks. These additional chambers deliver information with 15 to 25 ns time resolution which enables triggering and tagging of beam-crossings which happen at 25 ns intervals. The chambers that are used to achieve this are so called Resistive Plate Chambers (RPCs) in the barrel region which cover $|\eta|<1.05$ and in the end-cap region Thin Gap Chambers (TGCs) are used and cover $1.05<|\eta|<2.4$.

Figure 20: Schematic of muon spectrometer RPCs, From [23]

The RPC consists of three concentric cylindrical layers of gaseous parallel electrode-plate detectors, the two plates are made of phenolic-melanimic plastic laminate and are seperated by 2 mm of insulators. Like in the multi-wire proportional chambers the electric field forms an avalanche along ionizing tracks which will finally reach the anode and be read out. The gas used between the plates is C$_2$H$_2$F$_4$/Iso-C$_4$H$_{10}$/SF$_6$ in the ratio 94.7/5/0.3.

The TGC offers both a trigger signal as well as azimuthal coordinate measurements in order to complement the MDTs in the three outer end-cap wheels, where the MDTs are aligned radially. the TGCs are also gaseous detectors filled with a quenching gas mixture consisting of CO$_2$ and n-C$_5$H$_{12}$. The distance between the 50 μm wire and the cathode is here smaller than the wire-wire distance with 1.4 mm as compared to 1.8 mm. Through the combination of an operational voltage of 2900$\pm$100 V and the relatively small

wire-wire distance a relatively good time resolution is achieved for triggering.

Triggering of event recording

Because a bunch crossing happens every 25 ns at the LHC, the data rate would exceed the storage capabilities of the ATLAS experiment, if every bunch crossing was to be recorded. Because of this a two-level trigger system is implemented in order to only store the data of interest [33].

The Level-1 Trigger (L1) is implemented through hardware solutions by using a subset of the detector information in order to reduce the event rate from the bunch crossing rate to an event rate of 75 to 100 kHz. After an event is accepted by the L1, the events are then processed by the software based High Level Trigger (HLT) with an output rate of 1 kHz on average.

While it is important to make a fast decision, it is also important to take information from several parts of the detector in to account along with a variety of readout requirements, for example the time of flight of a charged particle to the muon spectrometer exceeds the time between bunch crossings, and a signal from the EM calorimeter extends over an amount of time equal to about four bunch crossings.

The multi-level triggering method along with local and central data buffers allows for the selection of interesting events while keeping a storage and bandwidth to a reasonable rate.

The L1 is implemented through custom electronics and is designed to accept signature of high p_T muons, electron/photon energy deposits, jets and hadronic decays of τ particles. In addition to particles it also accepts different thresholds of E_T^{miss} or large deposits of E_T.

In order to process the information fast, the L1 only handles a reduced subset of detector information, for muons this subset is the information from the RPC, TGC and in the muon spectrometer, for other signatures it is the EM calorimeter cluster information. The time restriction for the L1 is 2.5 μs after a bunch crossing, within this time frame the L1 needs to make a decision on whether to accept or reject an event, the ATLAS L1 has a target latency of 2 μs which means that the remaining 0.5 μs is a contingency, 1 μs of this processing time is spent on the signal traversing the wires, for this reason electronics handling the decision are as close to the subdetectors as possible, and the connection paths and cables are kept as short as possible.

The management of data and trigger information is handled by the Data Acquisition System (DAQ) which buffers the event data from subdetector specific readout electronics at the rate which the L1 provides the information. The data is buffered in pipeline memories and retained, which also happens close to the detector. The HLT then requests data depending on pre-defined regions of interest. If a region of interest passes the HLT, event-building is performed and passed by the DAQ to the event filter, if an event passes the HLT filter, the event then gets moved to the data storage and is recorded.

In order to make its decision the L1 menu has up to 256 items where each item is a rough requirement for the input data, this can take the form of the multiplicity of objects or flags indicating whether an event property such as E_T^{miss} has been passed, the HLT can then access further information from the spectrometers and calorimeters as well as combine this information with data from the inner detector in order to further specify the selection of data. This allows for finer targeting allowing for such things as reconstructing a b-decay, because of this the HLT needs more time decide whether or not to pass data and consists mostly of consumer networking hardware and computers, which makes it highly configurable.

The HLT takes about 500 ms to process an event, which reduces the event rate after the HLT decision to 1 kHz on average.

Object Definitions and truth matching

Object Definitions

In order to measure different particles at ATLAS we first need to define what their signatures should look like in the different parts of the detector, these definitions are based on recommendations from combined performance groups within the ATLAS experiment.

These Object Definitions make specific requirements for the kinematic properties of the track, the identification and isolation variables, as well as the impact parameters, for both electrons and muons.

In this section we will present the object definitions for electrons, muons and jets, as well as present the concept of E_{miss}^T (missing transverse energy), and the overlap removal procedure.

Electron reconstruction and identification

Since electrons traverse both the inner detector and the EM calorimeter and leave leave signals in both, electrons can be reconstructed by matching the tracks left in the inner detector with the energy clusters in the EM calorimeter. The Electron identification algorithm uses a likelihood based (LLH) method [34]. It is based on a multivariate analysis method which considers multiple properties of the potential electron candidate simultaneously, when determining the probability of whether the candidate is an electron or not. Different selection selection levels are defined using the algorithm, which vary in tightness based on changing the required efficiencies. For this thesis the DFCommonElectronsLHLoose selection was used, which requires a signal efficiency of 90% for electron candidates with transverse energy of roughly 25 GeV [35],[36]. With this selection electron candidates are also required to have a hit in the B-layer of the ID [34] in order to pass the selection. Additionally the candidate is required to pass certain requirements for pseudorapidity and transverse momentum. It has to have pt > 5 GeV and $|\eta| < 2.47$ with a veto in the calorimeter crack region, which is in the range $1.37<|\eta|<1.52$.

Muon reconstruction and identification

Muons are reconstructed from tracks in the inner detector along with hits in the muon spectrometer, as well as additional information gathered from deposits in the calorimeter. When a muon candidate has tracks in both the spectrometer and the inner detector, it is denoted as being combined. [37].

Jet reconstruction and identification

Jets traversing the detector are identified by using the bundles of tracks they leave in the inner detector along with the locally-calibrated topological clusters in the calorimeters using the anti-k_T algorithm with radius parameter $\Delta R = 0.4$ ($\Delta R = \sqrt{\Delta\eta^2 + \Delta\phi^2}$) [38],[39]. The requirements for the transverse momentum and pseudo rapidity of jets is $p_T > 20 GeV$ and $|\eta| > 4.5$.

Jets stemming from pileup are suppressed using selection based on a jet vertex tagger (JVT) algorithm [40]. This JVT algorithm is a tagging algorithm which identifies the jets coming from the hard scattering event, thereby rejecting jets stemming from pileup. Information from the tracks associated with the jets and information about the vertices are used in the algorithm. This applied JVT algorithm has a 92% efficiency in tagging jets and allows a 2% fake jet tagging rate from pileup jets.

Jets stemming from a b-quark have different properties compared to jets stemming from lighter quarks therefore a different algorithm is used to tag these b-jets. This algorithm uses a multi-variate approach to tag these relatively long live b-jets [41]. The working point for the b-tagging algorithm selection with efficiency 85% has been used in this analysis.

Tau identification

In order to identify tau leptons decaying hadronically something called the tau Boosted Decision Tree (tauBDT) is applied, this is an important process, as tau's hardly ever reach any of the detector layers of ATLAS, meaning that all tau's have to be reconstructed from their decay products, which makes them difficult to distinguish from jets. The tauBDT is a tool which combines several weaker classifying variables into a stronger discriminant for tau identification at ATLAS. The tauBDT is a machine learning algorithm

utilising a tree-like structure, it is structured such that a series of cuts and selections are applied to the tau candidate at each node of the tree, dependent on whether the candidate failed or passed the applied cuts it is passed on to one of two new nodes in the tree where new cuts are applied, and the candidate again moves to one of two nodes determined by whether it passed or failed the cut. No matter which direction the tau candidate takes through the tree, it will eventually reach a termination node, which determines the final BDTScore of the candidate, this score is between 0 and 1, with a higher score denoting a more likely tau candidate[42]. This BDT method has varying efficiency depending on how it decays, hadronically decaying taus decay to either one or three charged pions, which are identified with efficiencies of respectively 60% and 45%, with a misidentification rate of one in 70. For the backgrounds one in 84 and one in 700 fake taus pass the BDT selection with the same criteria.

Missing transverse energy

The missing transverse momentum P_T^{miss} with magnitude E_T^{miss} is defined as being the negative vector sum of the transverse momenta of all identified physics objects in an event along with an additional soft term [43]. The soft term includes all tracks in the detectors which are not associated with any specific physics objects but are still associated with the primary vertex. In order to get a good measurement it is very important to have a good suppression of pileup jets so as to not include momenta from previous events. E_T^{miss} is crucial in many analysis, as it is used to estimate the missing measurements from neutrinos as they do not interact with any of the detectors.

Overlap removal

Overlap removal is the process used in order to not count the same object twice when it is reconstructed as two different object types. Overlap removal between a jet and a lepton is done by looking at the angular separation $\Delta R = \sqrt{\Delta \eta^2 + \Delta \phi^2}$ between the reconstructed objects, along with their transverse momentum. Overlap removal between an electron and a muon is performed by comparing their tracks and not the angular separation.

Choice of final state for the search for Ns in the ATLAS experiment

In this thesis we have chosen to focus on the feasibility of the ATLAS experiment to be sensitive to the mixing of new heavy neutrinos with tau flavour neutrinos, since this has not been done before. The search focuses on a charged W boson decaying to a muon and an N, with the N decaying to a hadronically decaying tau, an electron and an electron neutrino, the feynman diagram for the channel is depicted in Figure 21. The reason for this choice is the initial study, described in this section, that showed that this channel is probably the only one ATLAS could detect in Run2, as it might have similar statistics as the channel studied in earlier searches for heavy neutral leptons, see the feynmann diagram shown in Figure 22.

The channel shown in Figure 21 is a new one not explored before in ATLAS, and it gives the best sensitivity to the mixing of N with tau neutrinos in Run2.
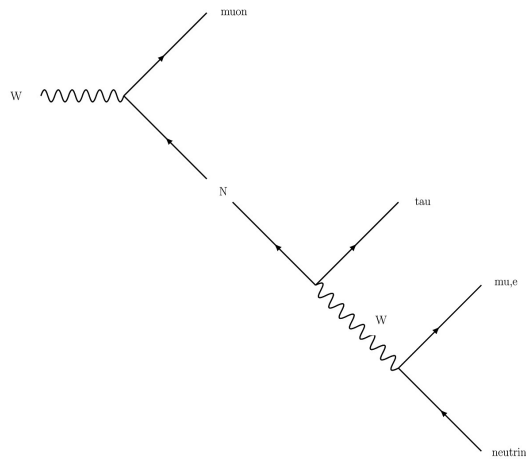
Figure 21: Feynmann diagram for the channel focus of this analysis (with N decaying into τ, e and ν_e
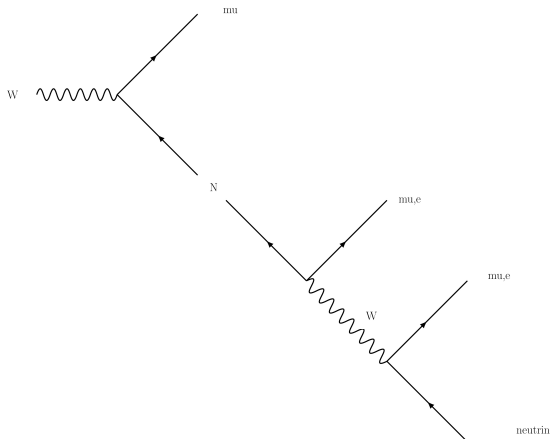
Figure 22: Feynmann diagram for the previously published search

The other channels which were considered are:

- The channel with the W decaying to a leptonically decaying tau and a N, with the N decaying to a muon and an electron along with the corresponding neutrino, depicted in Figure 23;

- The channel with the W decaying to a hadronic tau and a N, with the N decaying to a hadronic tau and an electron or muon along with the corresponding neutrino, depicted in Figure 24;

- the channel with the W decaying to a leptonically decaying tau and a N, with the N decaying to a hadronically decaying tau and muon or electron along with the corresponding neutrino, depicted in

Monte Carlo (MC) simulations are used to predict the way N's would appear, when produced in W decays from proton proton collisions. In particular the Monte Carlo generator program Pythia 8 [**?**] is used for simulating the main physics process, and is able also to simulate the part where quarks and gluons shower into softer particles and then hadronize.

A rough efficiency estimate for different channels is estimated in these MC simulations, for different masses of the N. When applying the criteria listed below, dependent on mass of the N, the number of initial events decreases. The numbers obtained are compared to the previously studied prompt muon channel depicted in Figure 22 which showed sensitivity and was used for an early publication. This should give an idea of which is the most promising channel for the study of tau mixing. This study is done at truth level, that means particle trajectories and energies are not smeared by the detector resolution. No identification or reconstruction efficiency is used. this is therefore a very optimistic study.

To be able to determine effects of N mixing with tau flavour, the hadronic decays of taus are the best to consider. Tau leptons decay roughly 65% of the times into hadrons (neutral or charged pions) and the remaining times into a electron or a muon. neutrinos always accompany the decay.

The selection criteria used are :

- All final state particles are required to have $|\eta| < 2.5$ because the tracking detector acceptance only covers that region.

- Prompt Leptonic $p_T > 26$ GeV (high pT, isolated, lepton originating from W). This criterion is determined by the single lepton trigger threshold, needed to save the data for analysis.

- Prompt Hadronic $p_T > 35$ GeV (high pT, isolated, lepton originating from W). This criterion is used only for the production mode depicted in Figure24, and is determined by the double-tau trigger threshold, needed to save the data for analysis.

For 10 GeV mass or lower for the N, a displaced vertex signature (long lived N) should be used to select the signal. For non yet excluded values of mixing vs mass in that region, the N will be long lived. We assume here this signature is so striking that it must be used to kill backgrounds, and allows to not ask for any identification of N decay products, thereby keeping the efficiency high.

In the low mass case, heavy neutral lepton decay products are identified through two particles with the requirements:

- Leading particle $p_T > 5$ GeV

- Sub-leading particle $p_T > 1$ GeV

assuming 100% efficiency to find a displaced vertex (optimistic assumption).

For high mass of the heavy neutral lepton (10 GeV or higher), the currently allowed mixing values make the N short lived, and therefore one cannot use anymore the displaced vertex signature. Therefore the identification criteria on the particles from the N decay are the following:

- Leading particle leptonic $p_T > 5$ GeV

- Sub-leading particle Hadronic tau $p_T > 25$ GeV or Sub-leading particle $p_T > 1$ GeV (if not tau lepton)
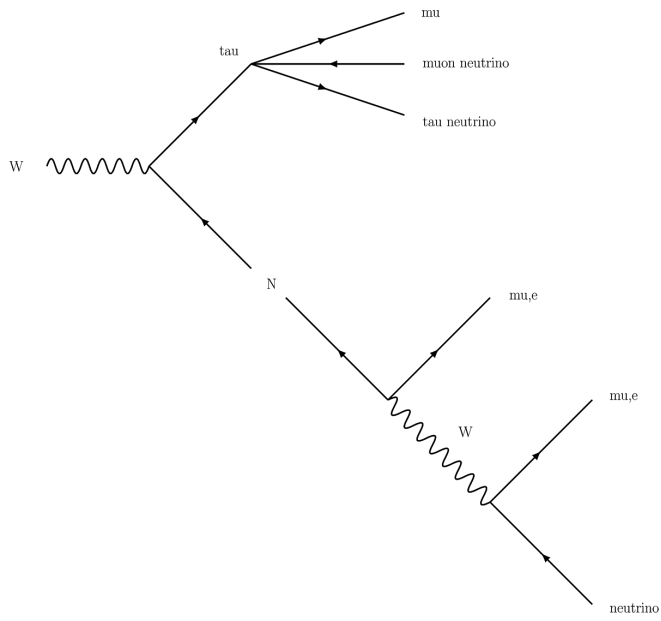
Figure 23: Feynmann diagram for channel with single leptonically decaying tau
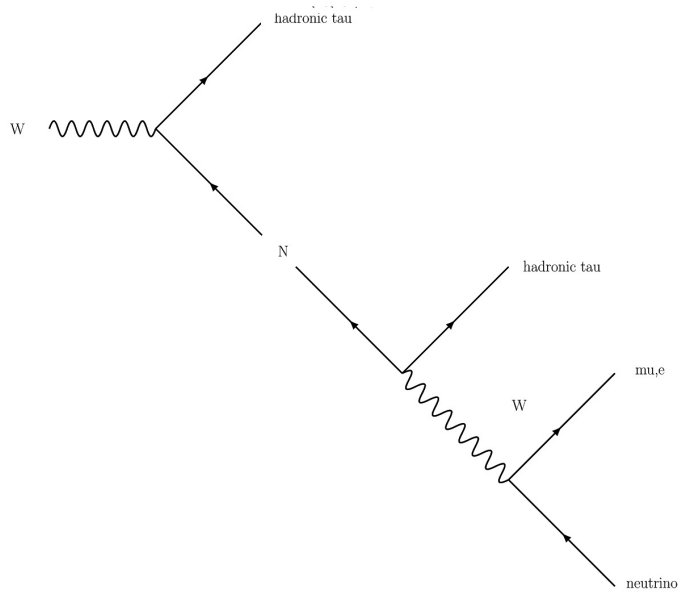

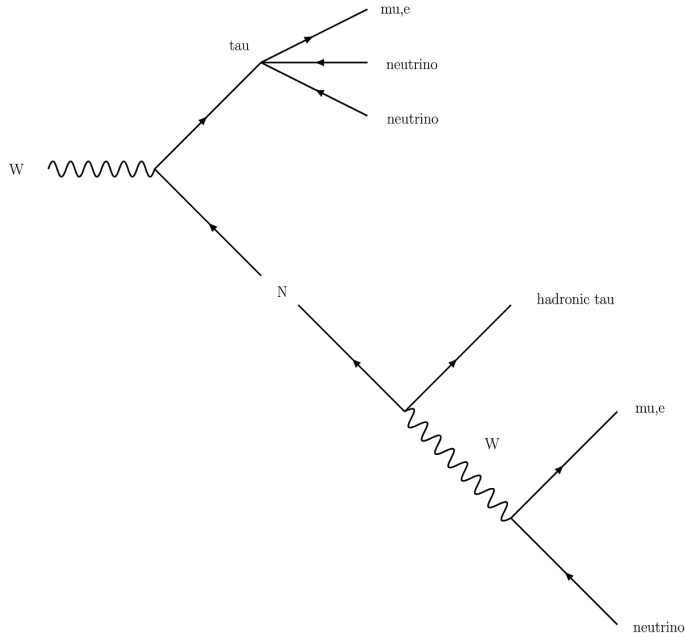Figure 24: Feynmann diagram for channel with two hadronically decaying taus

Figure 25: Feynmann diagram for channel with a leptonically decaying tau coming from the W and a hadronically decaying tau coming from the N

The requirements for ATLAS to identify a hadronically decaying tau are severe, starting from the request on the minimal value of p_T for the hadronic tau decays. Almost no events pass detection at either high or low mass of the heavy neutral lepton, for the production mode depicted in Figure 24.

At both high and low mass of the N, the tau coming from the W does not have enough p_T for its decay products to pass the 35 GeV threshold, as shown in Figure 26 for 10 GeV N mass and in Figure 27 for 60 GeV N mass.
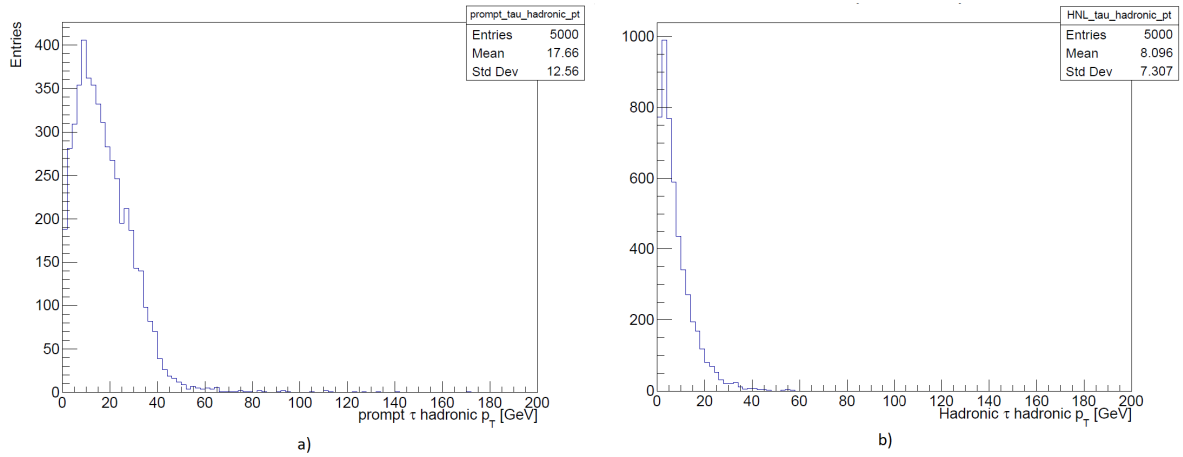
Figure 26: a) p_T of prompt tau hadronic decay with N mass set to 10 GeV b) p_T of the secondary tau with N mass set to 10 GeV
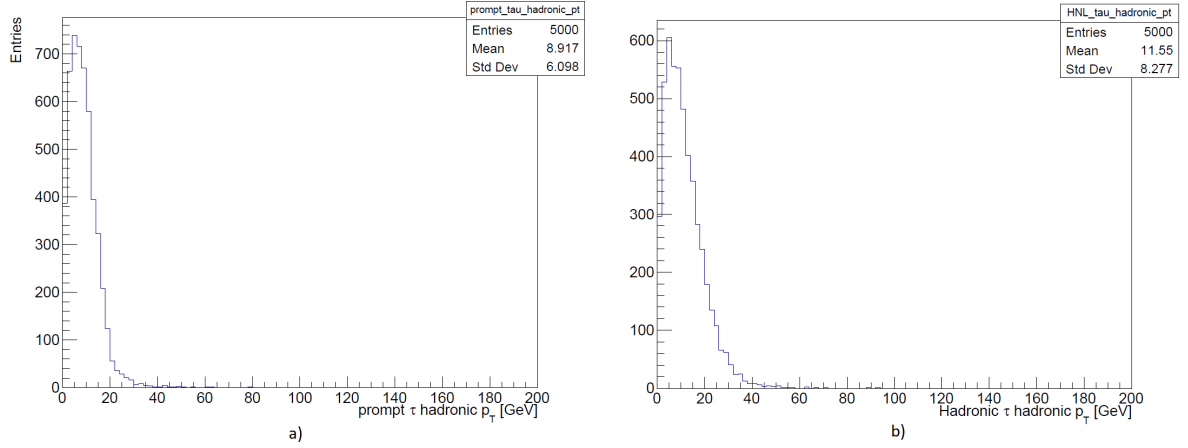
Figure 27: a) p_T of prompt tau hadronic decay with N mass set to 60 GeV b) p_T of the secondary tau with N mass set to 60 GeV

The channel with the W decaying to a leptonically decaying tau and the N decaying to a hadronically decaying tau as well as a muon or electron, feynmann diagram shown in Figure 25.

The requirements for identification of the prompt lepton of pT > 26 GeV almost entirely suppress detection at high mass points for the N as shown in Figure 28 which shows the p_T distribution of the leptons and the visible tau decay products for 60 GeV N mass.
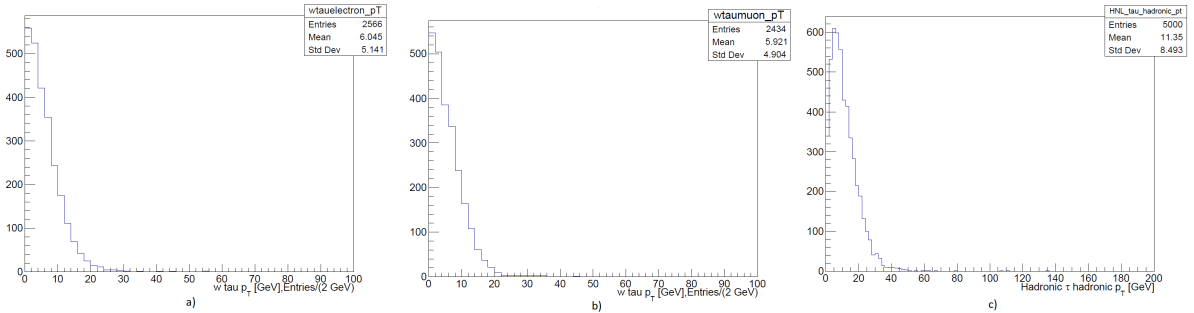
Figure 28: a) p_T of the prompt electron b) p_T of the leading muon c) p_T of the subleading tau, for N with mass set to 60 GeV

This channel does however seem to still have some chance to survive the data selection for low N mass case, where displaced vertex signature allows the requirement for identification of the N decay products to be lowered to having one track with $p_T > 5$ GeV and a second track with $p_T > 1$ GeV, this was tested with a simulation of a N with 10 GeV mass, with the results shown in Figure 29.
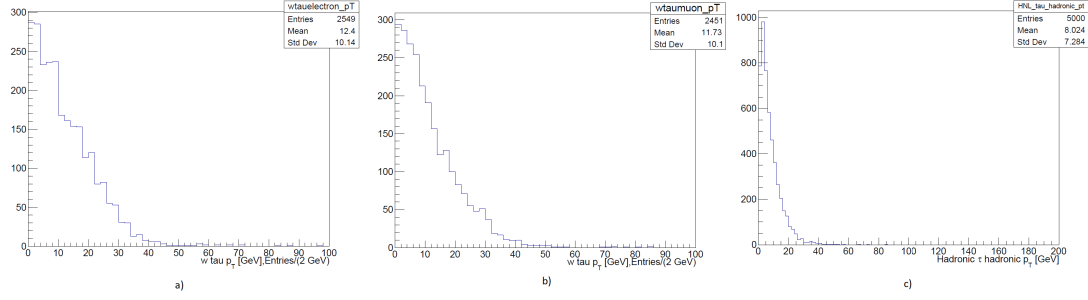
Figure 29: a) p_T of the prompt electron b) p_T of the leading muon c) p_T of the subleading tau for a N with mass set to 10 GeV

	reference channel	Prompt muon+hadronic	double hadronic	hadronic+leptonic.
Events passed (10 GeV)	704	580	34	88
Ratio with reference	1	0.824	0.0483	0.125
Events passed (60 GeV)	182	58	2	4
Ratio with reference	1	0.319	0.011	0.022

Table 2: Summary of results for truth analysis. Initial number of events generated for all channels is the same. The fraction of events passed by the selection, compared to the reference process , is listed, for two possible N masses.

From Table 2 we can see that for low masses of the N, the channel with a prompt muon and a hadronically decaying tau performs almost as well as the prompt muon reference channel, while also being comparable at high masses of the N. Conversely both the other channels considered are almost entirely suppressed by the detection criteria at ATLAS at any mass value of the N. Therefore for the rest of the work we focus on the process depicted in Figure 23.

Analysis strategy

HNL pseudo-Dirac or Majorana search

Heavy Neutral Leptons could manifest in the ATLAS experiment as a couple different types of particles. In this thesis we have selected to look at two possible options, namely the options of the HNL manifesting as a Majorana particle, see Figure 31 and as a pseudo-Dirac particle, see for example Figure 30.
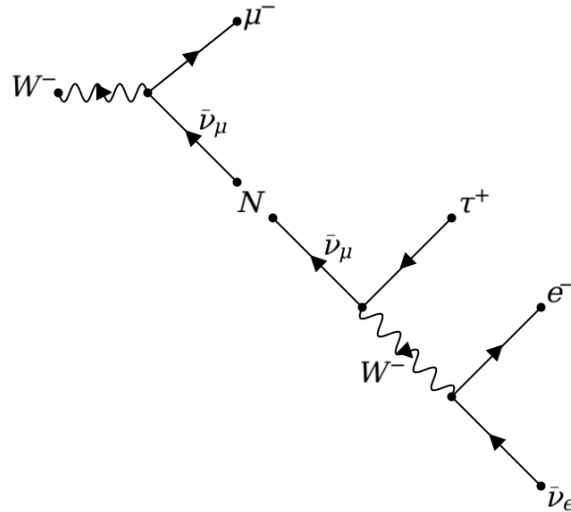
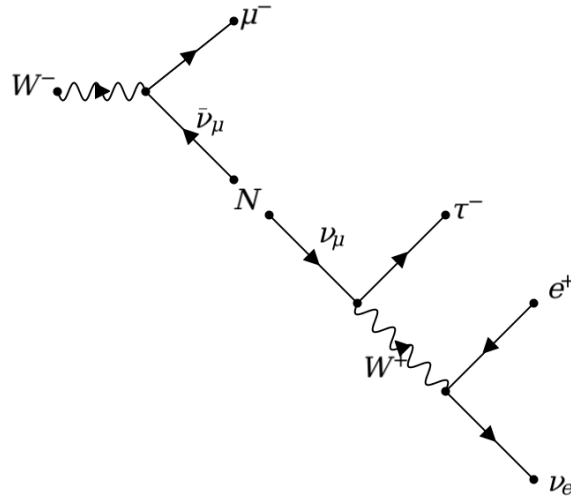Figure 30: Feynman diagram for pseudo-Dirac channel.

Figure 31: Feynman diagram for Majorana channel.

The way the two types of manifestations can be distinguished, is by looking at the charge of the tau compared to the muon. if they have the same sign, then it is a clear indication of the Majorana nature. If they are opposite sign, then the message is unclear, and it could actually be both types.
We will apply cuts to select the simulation for both cases, we will consider MC simulations for background processes, and will estimate the sensitivity to spot both cases, in $140\,\mathrm{fb}^{-1}$ data which accounts for the entire second run of the ATLAS experiment.

The MC simulations for the signal are similar to what was used in the previous chapter. The Pythia8 output is then sent into a Monte Carlo generator program called Geant4 [44] that simulates the particle interactions when crossing the material of the detector, leaving a signal.

Choice of background samples

When choosing which background channels to use in this analysis a couple of factors had to be considered, first of all we had to find background channels where the measured particles most closely mirror the measured particles in the final state in our signal.

This is however not an easy process because data from all such channels are not kept in an easily accessible format in ATLAS, there are however some channels for which data is generated in abundance, because they are the most abundantly produced backgrounds to most searches, such as the production of a top and anti–top quark, labelled as $t\bar{t}$, and the production of a W plus additional jets from high order corrections in the basic $pp \to W \to \mu N$ process, labelled as $W\mu\nu$, where the same particles are present as in the signal.

$t\bar{t}$ is a possible background for this search, because the final state for $t\bar{t}$ events contain three leptons, with one of them coming from a b-jet, making it very likely that $t\bar{t}$ events will contain all the requisite particles needed to be a good background sample for this search. The $t\bar{t}$ files used in this search are produced via a PowHeg MC generator [45], interfaced with Pythia8 [46] for the parton shower and hadronization process, and are represented by the feynman diagram of type shown in Figure 32.
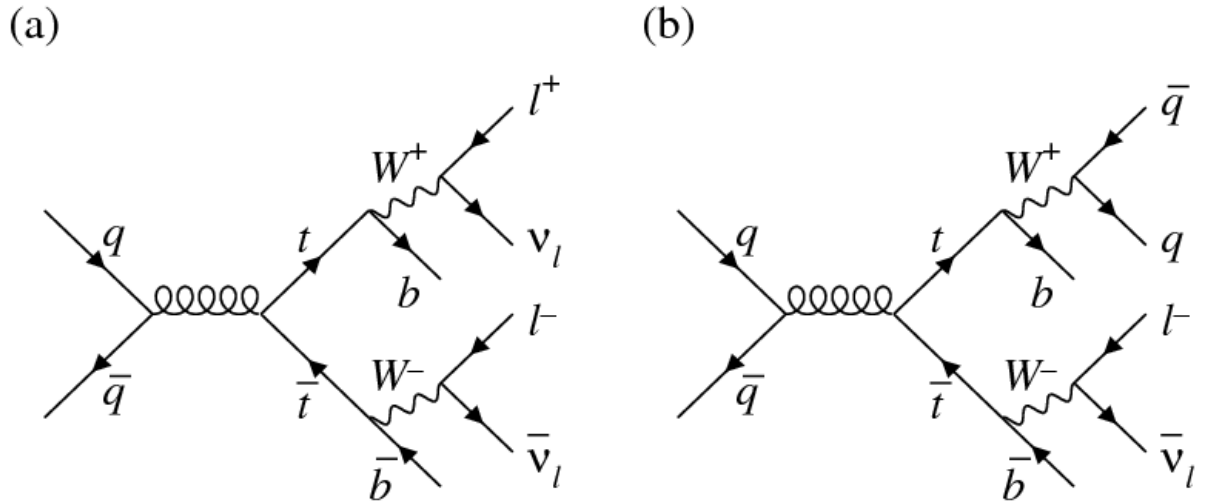

Figure 32: Feynman diagram for the $t\bar{t}$ background.

$W\mu\nu$ is a possible background for the search as it happens at the same production rate as the signal, and contains a muon coming from the W along with two "fake" electron and tau candidates stemming from jets, thus it also has the particles needed to be appearing as signal like. The $W\mu\nu$ background sample is generated using Sherpa [47] and are represented by the feynman diagram of type shown in Figure 33
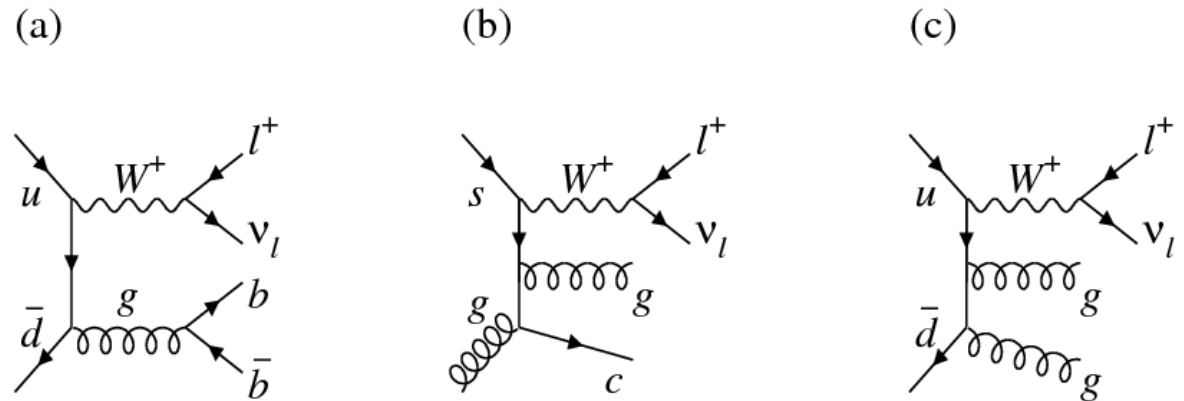

Figure 33: Possible Feynman diagrams for the $W\mu\nu$ plus jets background.

Both background samples are sent into a Monte Carlo generator program called Geant [?] that simulates

the particle interactions when crossing the material of the detector, leaving a signal.

This means that the study in this section becomes close to real data, and includes effects of detector resolution and reconstruction algorithms inefficiencies.

Selection

In order to determine the viability of studying the tau channel for Heavy neutral leptons, we need to apply a series of cuts and selections to both our own generated samples as well as to backgrounds with identical final state particles. The purpose of these cuts and selections is to cut down on background as efficiently as possible while retaining as much signal as possible. Some of the cuts and selection were also made in order to select the particles from our channel over particles generated from other processes.

We refer in the following to "Dirac criteria" as a selection where the muon and tau lepton are required to have opposite electric charge, and to "Majorana criteria" as a selection where the muon and tau lepton are required to have same electric charge.
A certain assignment of reconstructed leptons to fundamental particles at feynman diagram level is assumed, which of course can be optimized further in the future.

In order to accomplish this we made the following cuts and selection:

- First we require there to be no b-jets in the event, as b-jets should be very rare in the signal, while being abundant in the $t\bar{t}$ background and somewhat present in the W$\mu\nu$ background. the number of b-jets can be seen in Figure 34
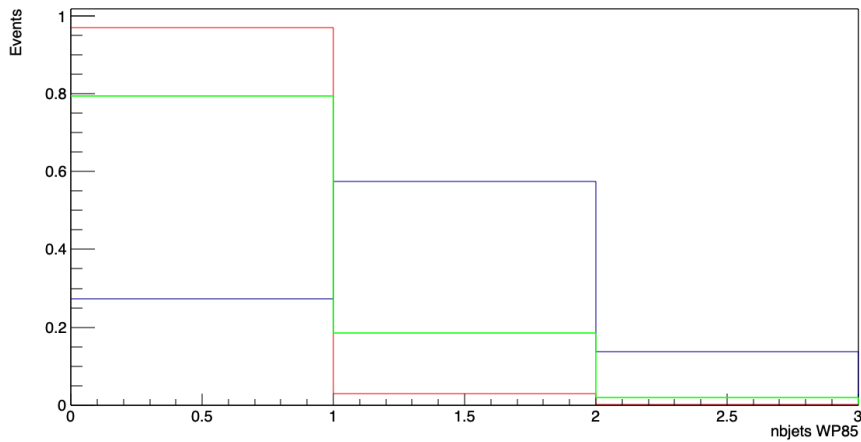

Figure 34: Number of b-jets present in signal and backgrounds. Red is the distribution for the 50 GeV Dirac channel, blue is the $t\bar{t}$ background with Dirac criteria and green is W$\mu\nu$ background with Dirac criteria

- Select the muon with the highest p_T as the prompt muon
  This assumes that the prompt muon (from W) is likely to be the most energetic muon.

- Require prompt muon p_T to be between 26 and 70 GeV
  The lower bound is set as it is the lowest detectable one for the prompt lepton, due to trigger requirements, while the higher bound is set as signal muons rarely have p_T's above this threshold while the background muons appear to be uniformly distributed even above this threshold. Examples of this are shown in Figure 35.
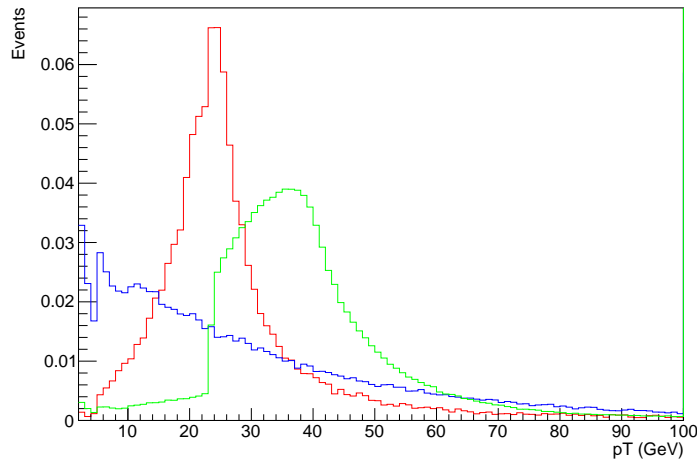
41

Figure 35: p_T distribution of muons. Red is the distribution for the 50 GeV N, blue is the $t\bar{t}$ background and green is W$\mu\nu$ background. Example taken from the Dirac criteria selection stage

- Select the subleading electron from N decay as the electron with the largest angular difference with respect to the muon and with the correct charge sign with respect to the muon (same for Dirac criteria and opposite for Majorana criteria)
  This electron is chosen as the electron and muon should theoretically be emitted in almost opposite directions (most W's are produced at rest, and decay products are back to back), thus the electron with the largest angular differential with respect to the muon is likely to be the electron that we are interested in studying.

- Apply Loose electron selection to this subleading electron

- Require electron p_T to be between 15 and 50 GeV
  Again the upper limit is based on the electron pt being distributed largely within this range for signal, while not being the case for the background samples as shown in Figure 36. The lower limit set here is actually above the detection threshold of 5 GeV for the secondary lepton, but this cut at 15 GeV was chosen as it has a small effect in filtering the signal, while being highly effective at removing the W$\mu\nu$ background.
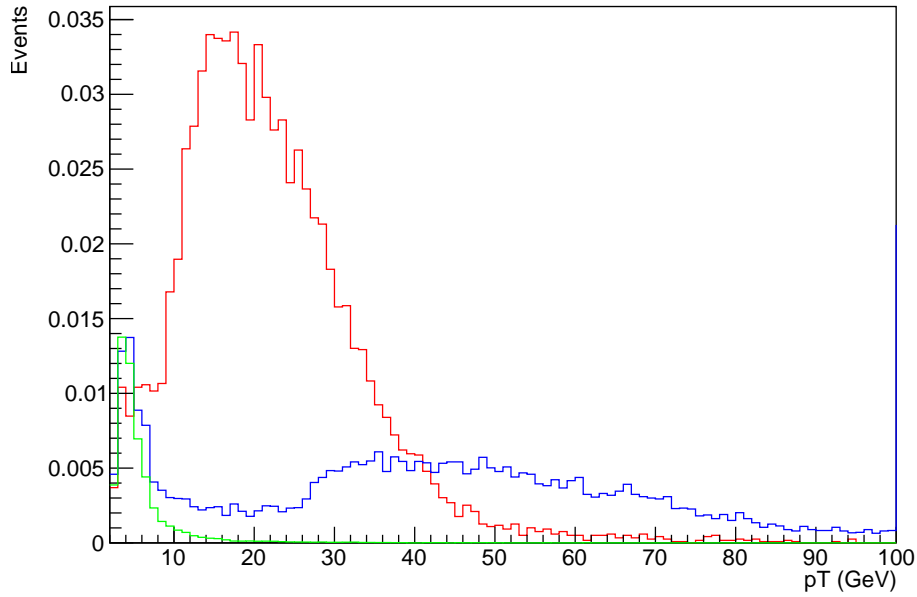
Figure 36: p_T distribution of electrons. Red is the distribution for the 50 GeV N, blue is for the $t\bar{t}$ background and green is the W$\mu\nu$ background. Example taken from the Dirac criteria selection stage

- Select the tau from N as the tau with the highest p_T and with the correct charge with respect to the muon (opposite for Dirac criteria and same for Majorana criteria)
  Like with the muon, we assume that the highest p_T tau is likely to be the one involved in the N decay we are interested in studying.

- Require tau p_T to be between 15 and 50 GeV
  Like with the other particles the upper limit is set as it more efficiently passes signal than background, as with the muon the lower limit is set at 15 GeV as it is the lowest required pt in order to detect taus.

- Require tau to have a tauBDT Score above 0.1. The tauBDT score cut is made since the variable is associated with the "realness" of taus, and it is assumed that the taus in our signal channel (real taus) are more likely to have high tauBDT score than those coming from the backgrounds. The efficiency of these cuts can be seen in Tables 6 and 7 and is visualised in Figure 37.
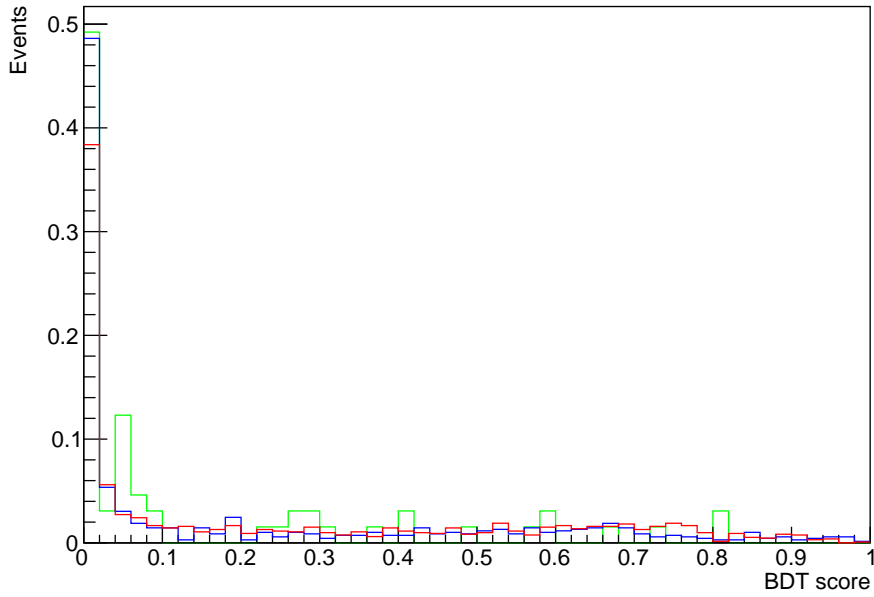
Figure 37: Distribution of tau BDT score. Red is the distribution for the 50 GeV N, blue is for the $t\bar{t}$ background and green is the W$\mu\nu$ background. Example taken from the Dirac criteria selection stage

- Require reconstructed mass of original W particle to be below 100 GeV and mass of the N to be below 70 GeV
  these cuts are made because the search focuses on real W and HNL produced, and the reconstructed masses of the decay products tend to be around the actual mass of the W and N respectively for the signal, while it is unlikely to have a good relation to these masses in the background, as the background particles are not likely to be the decay product of an on-mass-shell W boson and guaranteed not to be the decay products of a N. This can also be seen in Figures 38 and 39 for the M_N=50GeV case and in 40 and 52 for the M_N=20GeV case.
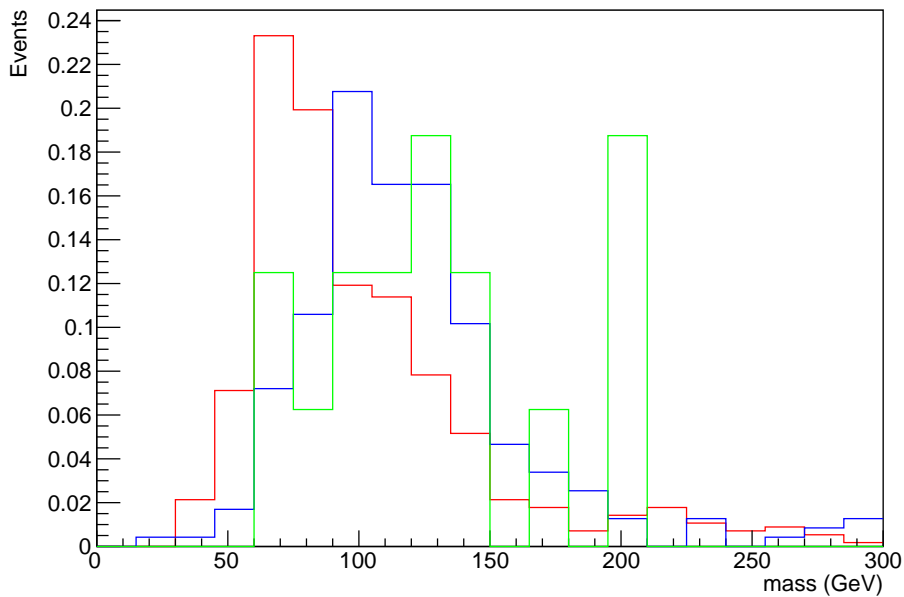

Figure 38: Reconstructed W masses. Red is the distribution for the 50 GeV N, Blue is the $t\bar{t}$ background and green is the W$\mu\nu$ background. Example taken from the Dirac criteria selection stage
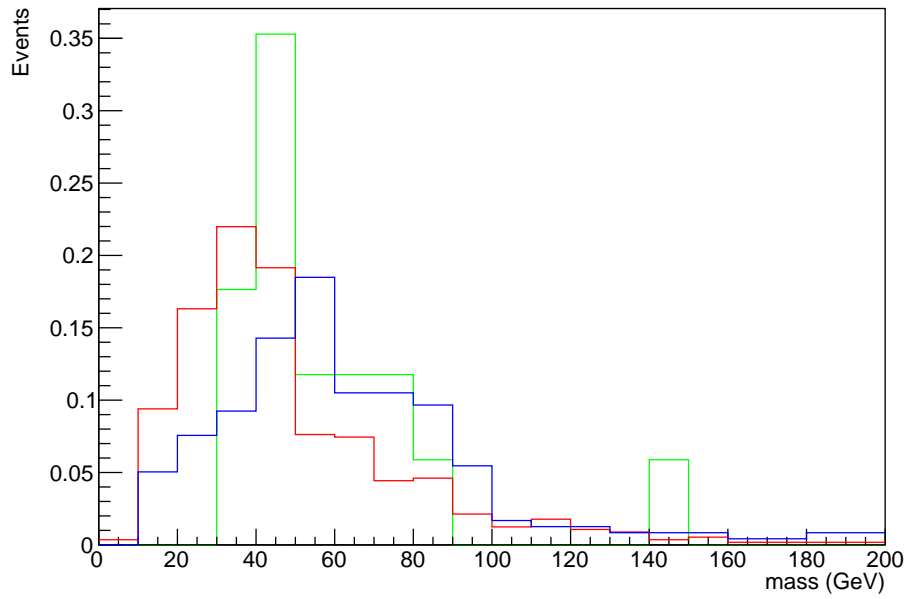
Figure 39: Reconstructed N masses. Red is the distribution for the 50 GeV N, blue is the $t\bar{t}$ background and green is the W$\mu\nu$ background. Example taken from the Dirac criteria selection stage
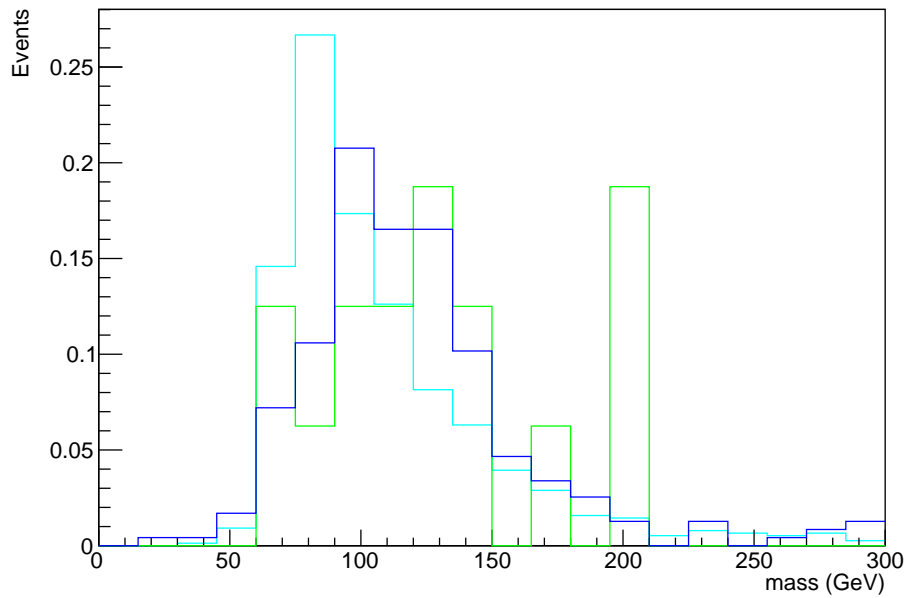

Figure 40: Reconstructed W masses. Cyan is the distribution for the 20 GeV Dirac N, blue is the $t\bar{t}$ background and green is W$\mu\nu$ background. Example taken from the Dirac criteria selection stage
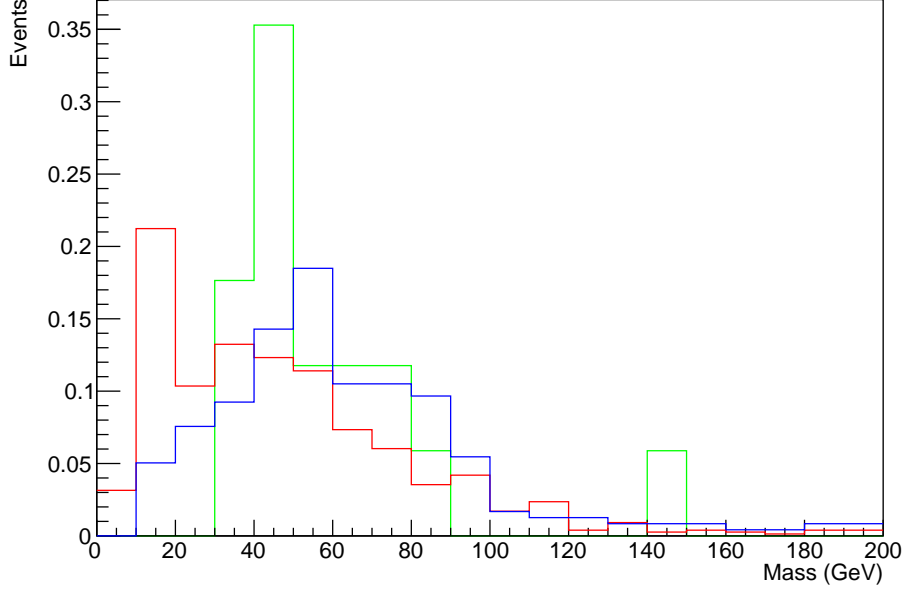
Figure 41: Reconstructed N masses. red is the distribution for the 20 GeV Dirac N, blue is the $t\bar{t}$ background and green is the W$\mu\nu$ background. Example taken from the Dirac criteria selection stage

The resulting efficiencies on signal and background simulated samples, when applying this selection procedure, is given in Table 6 and 7.

Expected number of events

In order to calculate how many events from the tau channel we expect to see at ATLAS we first need to calculate the cross section of the channel. This is done by first calculating the total width of the channel using eq. 28 from [48]

$$\Gamma(M_N, U_e^2, U_\mu^2, U_\tau^2) = \sum_{\alpha=e,\mu,\tau} U_\alpha^2 \times \hat{\Gamma}_\alpha(M_N) \tag{28}$$

Once the total Width has been calculated, it is then rescaled in order to obtain the cross section for the channel using eq. 29

$$\sigma(M_N, U_e^2, U_\mu^2, U_\tau^2) = \sigma_P^{ref}(M_N) \times \frac{U_{\alpha(P)}^2 U_{\beta(P)}^2}{U_{ref}^4} \times \frac{\Gamma_{ref}}{\Gamma(M_N, U_e^2, U_\mu^2, U_\tau^2)} \tag{29}$$

Here U_α^2 is the mixing angle, which has been chosen arbitrarily from Figure 42 to be, $\frac{U_e^2}{U^2}$=0, $\frac{U_\mu^2}{U^2}$=0.5 and $\frac{U_\tau^2}{U^2}$=0.5, with $U_\tau^2 = 10^{-5}$.

The parameters U_{ref} and Γ_{ref} are fixed parameters for the mixing angles and width, which are introduced in order to give the correct scale to the calculations.

$\Gamma(M_N, U_e^2, U_\mu^2, U_\tau^2)$ is the result of the previous equation, Γ_{ref}=10^{-5} GeV, the values of $\hat{\Gamma}_\alpha$ and $\sigma_P^{ref}(M_N)$ depend on the mass of the N, and whether the channel has a Majorana or Dirac N and are given in Table 3.
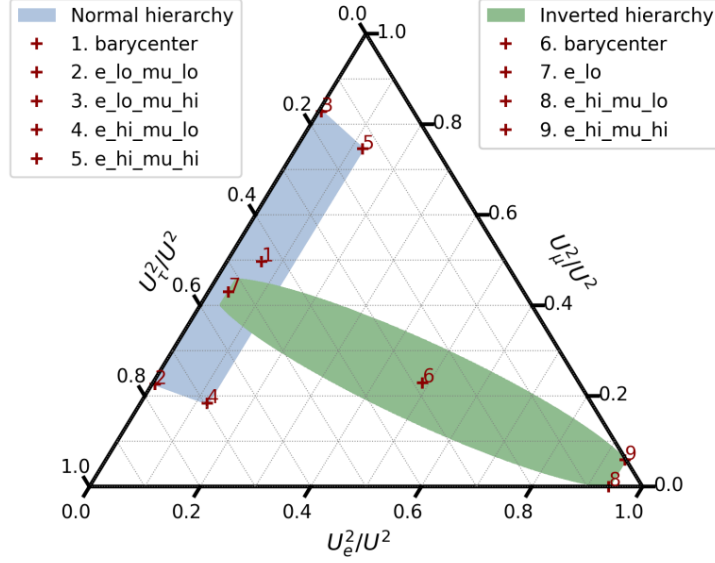
Figure 42: Figure of possible neutrino mixing angles values, from [49]

Figure 42 shows which mixing angles are allowed in the type 1 seesaw mechanism theory. The shaded regions represent which values for the mixing angles are allowed depending on whether the neutrino mass hierarchy is the normal (blue) or inverse (green) hierarchy. The marked points represent different variations of neutrino mass orderings in the two possible hierarchies [49].

	20 GeV	50 GeV
$\hat{\Gamma}_e$	$1.903254 \cdot 10^{-6} GeV$	0.0002317007 GeV
$\hat{\Gamma}_\mu$	$1.901958 \cdot 10^{-6}$ GeV	0.0002314281 GeV
$\hat{\Gamma}_\tau$	$1.901892 \cdot 10^{-6}$ GeV	0.0002316806 GeV
$\Gamma(M_N, U_e^2, U_\mu^2, U_\tau^2)$	$3.8 \cdot 10^{-11}$ GeV	$4.64 \cdot 10^{-9}$ GeV
σ_P^{ref}	218 pb	6550 pb
$\sigma_P(M_N, U_e^2, U_\mu^2, U_\tau^2)$	$5.74 \cdot 10^{-3}$ pb	$2.83 \cdot 10^{-3}$ pb

Table 3: Values of widths and cross sections for each channel analysed [48]

When the cross section is known, the expected amount of events can be calculated by eq. 30

$$n_{truth} = integrated - luminosity \times \sigma_P(M_N, U_e^2, U_\mu^2, U_\tau^2) \times Br(\tau \to hadrons + \nu_\tau) \quad (30)$$

Where $Br(\tau \to hadrons + \nu_\tau)$=0.65.

The number n_{truth} is the total number of events from our channel expected to occur in ATLAS, without any detector or reconstruction efficiency loss. A more interesting number for this analysis however, is the number of events that we can actually detect at ATLAS, in order to get this number we use eq 31.

$$n_{selected} = n_{truth} \times eff_{gen} \times eff_{DAOD} \times eff_{selection} \quad (31)$$

where eff is short for efficiency, from respectively the generator level, the data format (DAOD) conversion filtering, and lastly from the selection we apply to the data. The generator and DAOD efficiencies are listed in Table 4 and 5 and the selection efficiency is shown in Tables 6 and 7.

	20 GeV Pseudo-Dirac	50 GeV Pseudo-Dirac	20 GeV Majorana	50 GeV Majorana
eff_{gen}	0.405877	0.502058	0.411218	0.494707
eff_{DAOD}	0.429225	0.4359875	0.430025	0.4380625

Table 4: MC generator and DAOD filter efficiencies for signal MC samples

	$t\bar{t}$	$W\mu\nu$
eff_{gen}	0.54382	0.0655
eff_{DAOD}	0.4546	0.06

Table 5: MC generator and DAOD filter efficiencies for background MC samples

Cut/Selection	20 GeV	50 GeV	$t\bar{t}$	$W\mu\nu$
No cut	1	1	1	1
no b-jets	0.97	0.97	0.2	0.8
Mu pt > 26 GeV	0.755	0.342	0.306	0.768
Electron selection	0.796	0.788	0.352	0.0518
Electron pt > 15 GeV	0.632	0.625	0.193	0.015
Tau Charge requirement	0.241	0.337	0.645	0.487
Tau pt > 15 GeV	0.636	0.668	0.472	0.448
Tau BDT score > 0.1	0.386	0.423	0.346	0.262
W mass < 100 GeV N mass < 70 GeV	0.534	0.603	0.343	0.176
Total efficiency	0.0116	0.00937	0.000151	$4.81 \cdot 10^{-6}$

Table 6: Table of the efficiency of cuts and selection on signal and background with a Dirac criteria selection

Cut/Selection	20 GeV	50 GeV	$t\bar{t}$	$W\mu\nu$
No cut	1	1	1	1
No b-jets	0.97	0.97	0.2	0.8
Mu pt > 26 GeV	0.749	0.339	0.306	0.768
Electron selection	0.789	0.736	0.333	0.0473
Electron pt > 15 GeV	0.641	0.68	0.442	0.0176
Tau Charge requirement	0.324	0.384	0.637	0.514
Tau pt > 15 GeV	0.416	0.515	0.353	0.378
Tau BDT score > 0.1	0.365	0.411	0.36	0.242
W mass < 100 GeV N mass < 70 GeV	0.541	0.675	0.297	0.267
Total efficiency	0.00978	0.00902	0.000217	$6.41 \cdot 10^{-6}$

Table 7: Table of the efficiency of cuts and selection on signal and background with a Majorana criteria selection

	$t\bar{t}$	$W\mu\nu$
Cross section	730 pb	20 nb
eff_{gen}	0.54382	0.0655
eff_{DAOD}	0.4546	0.006

Table 8: Table of generation and DAOD efficiency for backgrounds

In order to calculate the amount of events we can expect to detect from the backgrounds we also include a table of the cross section of the backgrounds, shown in Table 8, needed as well as Table 5.

Now that we have all the relevant variables, we can calculate the expected number of truth and selected events, results of which are shown in Tables 9 and 10.

Expected number of events	20 GeV	50 GeV	$t\bar{t}$	$W\mu\nu$
Truth events in 140 fb^{-1}	522.34	262.99	$1.02 \cdot 10^{8}$	$2.8 \cdot 10^{9}$
Selected events in 140 fb^{-1}	1.056	0.528	3677	5.3

Table 9: Table of expected number of events for signal and background with a Dirac criteria selection

In order to understand how these numbers translate into the possibility of discovering N's it is relevant to look at the signal of background ratio $\frac{S}{\sqrt{B}}$ presented for each case in Table 11, where B is the total number of background events left for the two background processes considered.

These values of $\frac{S}{\sqrt{B}}$ are much too low to have any hope of making a discovery in the data collected

Expected number of events	20 GeV	50 GeV	$t\bar{t}$	W$\mu\nu$
Truth events in 140 fb^{-1}	522.34	262.99	$1.02 \cdot 10^8$	$2.8 \cdot 10^9$
Selected events in 140 fb^{-1}	0.901	0.504	5284	7.06

Table 10: Table of expected number of events for signal and background with a Majorana criteria selection

	20 GeV Dirac	50 GeV Dirac	20 GeV Majorana	50 GeV Majorana
$\frac{S}{\sqrt{B}}$ in 140 fb^{-1}	0.0174	0.0087	0.0124	0.00693

Table 11: Table of ratio of signal over background events, for all analysed channels, after selection

during the LHC Run2, in order to have a certain discovery we would need a $\frac{S}{\sqrt{B}}$ of 5 or above, meaning that in order to discover an N with this selection strategy we would an integrated luminosity approximately 500 times higher.

Future improvements on selection

The selection applied in this thesis can potentially be improved upon in several different ways. In this section, some of these potential improvements are outlined.

In this thesis the same selection strategy has been applied to all data regardless of which N mass was studied, this is not the optimal approach, as the cuts and selections could be tuned to each masspoint for the N in order to both increase the amount of signal passing selection as well as reducing the amount of background passing selection.
An example of how this could be done, would be that for the 20 GeV N samples, prompt muons have a higher average p_T compared to the 50 GeV N samples, so the cuts could be more accurately tuned to the expected muon p_T for each case. The assignment of which is the muon from the W could include for example other variables, to make the assignment more correct, for a given mass.

Another example of what could be improved would be to target the electron as the prompt lepton, this could help as the ATLAS detection criteria for identification of a prompt lepton, require either the muon or the electron to have a p_T above 26 GeV while the other lepton only needs to have a p_T above 5 GeV, thus the efficiency of the selection could conceivably be improved, by allowing either of the leptons to be the prompt lepton, as opposed to how we have done it where we always treat the muon as the prompt lepton which is forced to carry the higher p_T.
Since we want to be sensitive to mixing to tau leptons, testing the data for the hypothesis where the mixing with electron neutrinos is also nonzero should be usefull additional information.

In this search we also restricted the selection applied to electrons to the loose selection, where applying a tighter selection would cut down significantly on the W$\mu\nu$ background, and could conceivably also reduce the amount of $t\bar{t}$ background passing selection by a significant amount.

Additionally we could apply isolation criteria to leptons, which would help in getting better lepton candidates making it both more likely that we pick the correct particles, as well as reducing the number of "fake" leptons from the background.

Another useful quantity which can be added to the analysis would be the E_{miss}^T, which could be a good discriminator, as although there are two final state neutrinos in our signal, there could still be less E_{miss}^T in the signal, compared to the backgrounds. Including E_{miss}^T in the invariant mass calculations for both the W and the N, should also provide more precise masses making it easier to use it to make cuts based on the invariant mass.

The tails in both the invariant masses of the N's and W's, might also suggest that the correct particles are not necessarily chosen for each event in the analysis, suggesting that a more sophisticated process is needed when choosing which particles are assigned to W and N as their decay products.

References

[1] MissMj. Standard model of elementary particles.svg - wikipedia, the free encyclopedia. URL https://en.wikipedia.org/wiki/File:Standard_Model_of_Elementary_Particles.svg.

[2] Creative commons license. version cc by 3.0 free software foundation. URL https://creativecommons.org/licenses/by/3.0/deed.en.

[3] Jeffrey Goldstone, Abdus Salam, and Steven Weinberg. Broken symmetries. *Phys. Rev.*, 127:965–970, Aug 1962. doi: 10.1103/PhysRev.127.965. URL https://link.aps.org/doi/10.1103/PhysRev.127.965.

[4] Amit Roy. Helicity of the neutrino. *Resonance*, 6:32–43, Aug 2001. URL https://www.ias.ac.in/article/fulltext/reso/020/08/0699-0710.

[5] Y. Fukuda et al The Super-Kamiokande Collaboration. Evidence for oscillation of atmospheric neutrinos. *Phys.Rev.Lett.81:1562-1567,1998*. doi: 10.1103/PhysRevLett.81.1562. URL https://arxiv.org/abs/hep-ex/9807003.

[6] SNO Collaboration. Measurement of the total active 8b solar neutrino flux at the sudbury neutrino observatory with enhanced neutral current sensitivity. *Phys.Rev.Lett.92:181301,2004*, . doi: 10.1103/PhysRevLett.92.181301. URL https://arxiv.org/abs/nucl-ex/0309004.

[7] KamLAND Collaboration. A high sensitivity search for $\bar{\nu}_e$'s from the sun and other sources at kamland. *Phys.Rev.Lett.92:071301,2004*, . doi: 10.1103/PhysRevLett.92.071301. URL https://arxiv.org/abs/hep-ex/0310047.

[8] M. et al Tanabashi. Review of particle physics. *Phys. Rev. D*, 98:030001, Aug 2018. doi: 10.1103/PhysRevD.98.030001. URL https://link.aps.org/doi/10.1103/PhysRevD.98.030001.

[9] Kismalac. Neutrino mass hierarchy - wikipedia, the free encyclopedia. URL https://commons.wikimedia.org/wiki/File:NeutrinoHierarchy.svg.

[10] Oleg Ruchayskiy Alexey Boyarsky and Mikhail Shaposhnikov. The role of sterile neutrinos in cosmology and astrophysics. *Ann. Rev. Nucl. Part. Sci.59 (2009), pp. 191–214*. doi: 10.1146/annurev.nucl.010909.083654. URL https://www.annualreviews.org/doi/10.1146/annurev.nucl.010909.083654.

[11] W et al Bonivento. Proposal to search for heavy neutral leptons at the sps. URL https://cds.cern.ch/record/1606085/files/nuMSM+H_LR.png.

[12] B. Gripaios. Gauge field theory. lecture notes: Gauge field theory at university of cam-bridge part iii natural sciences tripos. 2017.

[13] A. Strumia and F. Vissani. Neutrino masses and mixings and... *ArXiv High EnergyPhysics(2006).*

[14] Oleg Ruchayskiy and Artem Ivashko. Experimental bounds on sterile neutrino mixing angles. *JHEP 1206*, 2012. doi: 10.1007/JHEP06(2012)100. URL https://arxiv.org/abs/1112.3319.

[15] Sergey Alekhin et al. A facility to search for hidden particles at the cern sps: the ship physics case. *Rep. Prog. Phys. 79 (2016) 124201*, . doi: 10.1088/0034-4885/79/12/124201. URL https://arxiv.org/abs/1504.04855.

[16] CMS collaboration. Search for heavy majorana neutrinos in $\mu^\pm\mu^\pm+$ jets events in proton–proton collisions at s=8 tev. *Physics Letters B*, 748:144–166, 2015. ISSN 0370-2693. doi: https://doi.org/10.1016/j.physletb.2015.06.070. URL https://www.sciencedirect.com/science/article/pii/S0370269315005006.

[17] The ATLAS Colaboration. Search for heavy neutral leptons in decays of w bosons produced in 13 tev pp collisions using prompt and displaced signatures with the atlas detector. *Journal of High Energy Physics volume 2019, Article number: 265 (2019)*. URL https://link.springer.com/article/10.1007/JHEP10(2019)265#citeas.

[18] Oliver Sim et al Brüning. Lhc design report. doi: 10.5170/CERN-2004-003-V-1. URL https://cds.cern.ch/record/782076.

[19] Esma Mobs. The cern accelerator complex. URL https://cds.cern.ch/record/2197559.

[20] ATLAS colaboration. rendering of atlas detector. URL https://atlas.cern/discover/detector.

[21] G Aad et al. Atlas pixel detector electronics and sensors. *Journal of Instrumentation, Volume 3, July 2008*, . URL https://iopscience.iop.org/article/10.1088/1748-0221/3/07/P07007.

[22] Joao Pequenao. Computer generated image of the atlas inner detector. URL https://cds.cern.ch/images/CERN-GE-0803014-01.

[23] O Abdinov et al. The atlas experiment at the cern large hadron collider. *Journal of Instrumentation, Volume 3, August 2008*, . URL https://iopscience.iop.org/article/10.1088/1748-0221/3/08/S08003.

[24] Gunnar Lindström. Radiation damage in silicon detectors. *Nuclear Instruments and Methods in Physics Research Section A: Accelerators, Spectrometers, Detectors and Associated Equipment*, 512(1):30–43, 2003. ISSN 0168-9002. doi: https://doi.org/10.1016/S0168-9002(03)01874-6. URL https://www.sciencedirect.com/science/article/pii/S0168900203018746. Proceedings of the 9th European Symposium on Semiconductor Detectors: New Developments on Radiation Detectors.

[25] M. Capeans et al. Atlas insertable b-layer technical design report. . URL https://cds.cern.ch/record/1291633.

[26] K. Hanagaki. Atlas silicon microstrip tracker operation. *Nuclear Instruments and Methods in Physics Research Section A: Accelerators, Spectrometers, Detectors and Associated Equipment*, 636(1, Supplement):S173–S176, 2011. ISSN 0168-9002. doi: https://doi.org/10.1016/j.nima.2010.04.105. URL https://www.sciencedirect.com/science/article/pii/S0168900210009599. 7th International ""Hiroshima"" Symposium on the Development and Application of Semiconductor Tracking Detectors.

[27] CERN. Geneva. LHC Experiments Committee ; LHCC. Atlas liquid-argon calorimeter : Technical design report. *Geneva : CERN, 1996. - 606 p.*, . URL https://cds.cern.ch/record/331061.

[28] CERN. Geneva. LHC Experiments Committee ; LHCC. Atlas tile calorimeter : Technical design report. *Geneva : CERN, 1996. - 333 p.*, . URL https://cds.cern.ch/record/331062.

[29] ATLAS TileCal Collaboration. Design, construction and installation of the atlas hadronic barrel scintillator-tile calorimeter. . URL https://cds.cern.ch/record/1071921.

[30] A Artamonov et al. The atlas forward calorimeter. . URL https://iopscience.iop.org/article/10.1088/1748-0221/3/02/P02010.

[31] A. Yamamoto et al. The atlas central solenoid. *Nuclear Instruments and Methods in Physics Research Section A: Accelerators, Spectrometers, Detectors and Associated Equipment*, 584(1):53–74, 2008. ISSN 0168-9002. doi: https://doi.org/10.1016/j.nima.2007.09.047. URL https://www.sciencedirect.com/science/article/pii/S0168900207020414.

[32] D. E. Baynham, J. Butterworth, F. S. Carr, M. J. D. Courthold, D. A. Cragg, C. J. Densham, D. Evans, E. Holtom, J. Rochford, D. Sole, E. F. Towndrow, and G. P. Warner. Engineering status of the superconducting end cap toroid magnets for the atlas experiment at lhc. *IEEE Transactions on Applied Superconductivity*, 10(1):357–360, 2000. doi: 10.1109/77.828247.

[33] M. Aaboud et al Atlas Collaboration. Performance of the atlas trigger system in 2015. *The European Physical Journal C volume 77, Article number: 317 (2017)*. URL https://link.springer.com/article/10.1140%2Fepjc%2Fs10052-017-4852-3.

[34] The ATLAS collaboration. Electron efficiency measurements with the atlas detector using the 2012 lhc proton-proton collision data. . URL https://cds.cern.ch/record/1706245.

[35] The ATLAS collaboration. Electron efficiency measurements with the atlas detector using the 2012 lhc proton-proton collision data. . URL https://cds.cern.ch/record/1706245.

[36] The ATLAS collaboration. Lowest un-prescaled triggers per data-taking period. . URL https://twiki.cern.ch/twiki/bin/viewauth/Atlas/LowestUnprescaled.

[37] The ATLAS collaboration. Muon reconstruction performance in early $\sqrt{s}$ = 13 tev data. . URL https://cds.cern.ch/record/2047831.

[38] The ATLAS collaboration. Jet calibration and systematic uncertainties for jets reconstructed in the atlas detector at $\sqrt{s}$=13 tev. . URL https://cds.cern.ch/record/2037613.

[39] Gavin P. Salam Matteo Cacciari and Gregory Soyez. The anti-k_t jet clustering algorithm. *Journal of High Energy Physics, Volume 2008, JHEP04(2008)*. URL https://iopscience.iop.org/article/10.1088/1126-6708/2008/04/063.

[40] The ATLAS collaboration. Tagging and suppression of pileup jets. . URL http://cdsweb.cern.ch/record/1643929.

[41] M. Aad G. et al. The ATLAS collaboration., Aaboud. Measurements of b-jet tagging efficiency with the atlas detector using t$\bar{t}$ events at $\sqrt{s}$=13 tev. doi: https://doi.org/10.1007/JHEP08(2018)089.

[42] Jennifer Godfrey. Using boosted decision trees for tau identification in the atlas experiment. URL https://www.yumpu.com/en/document/read/37894844/using-boosted-decision-trees-for-tau-identification-in-the-atlas-.

[43] ATLAS Collaboration. Performance of missing transverse momentum reconstruction with the atlas detector using proton-proton collisions at $\sqrt{s}$ = 13 tev. *Eur. Phys. J. C 78 (2018) 903*. doi: 10.1140/epjc/s10052-018-6288-9. URL https://arxiv.org/abs/1802.08168.

[44] S. Agostinelli et al. Geant4—a simulation toolkit. *Nuclear Instruments and Methods in Physics Research Section A: Accelerators, Spectrometers, Detectors and Associated Equipment*, 506(3):250–303, 2003. ISSN 0168-9002. doi: https://doi.org/10.1016/S0168-9002(03)01368-8. URL https://www.sciencedirect.com/science/article/pii/S0168900203013688.

[45] C. Oleari. The powheg box. *Nuclear Physics B - Proceedings Supplements*, 205-206:36–41, 2010. ISSN 0920-5632. doi: https://doi.org/10.1016/j.nuclphysbps.2010.08.016. URL https://www.sciencedirect.com/science/article/pii/S0920563210001994. Loops and Legs in Quantum Field Theory.

[46] Torbjörn Sjöstrand. The pythia event generator: Past, present and future. doi: 10.1016/j.cpc.2019.106910. URL https://arxiv.org/abs/1907.09874.

[47] T Gleisberg, S Höche, F Krauss, M Schönherr, S Schumann, F Siegert, and J Winter. Event generation with SHERPA 1.1. *Journal of High Energy Physics*, 2009(02):007–007, feb 2009. doi: 10.1088/1126-6708/2009/02/007. URL https://doi.org/10.1088/1126-6708/2009/02/007.

[48] Jean-Loup Tastet. Reinterpreting the atlas limits on hnls: preliminary results and lessons learned. jan 2021.

[49] J. Lopez-Pavon J. Salvado A. Caputo, P. Hernandez. The seesaw portal in testable models of neutrino masses. doi: 10.1007/JHEP06(2017)112. URL arXiv:1704.08721.

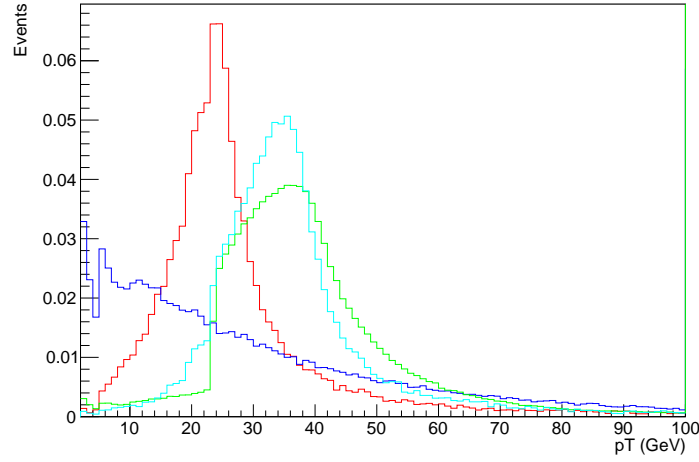# Appendices

p_T distributions

Figure 43: p_T distribution of muons for Dirac channel. Cyan is the distribution for the 20 GeV Dirac channel, red is the 50 GeV Dirac channel, blue is the $t\bar{t}$ background with Dirac criteria and green is the W$\mu\nu$ background with Dirac criteria
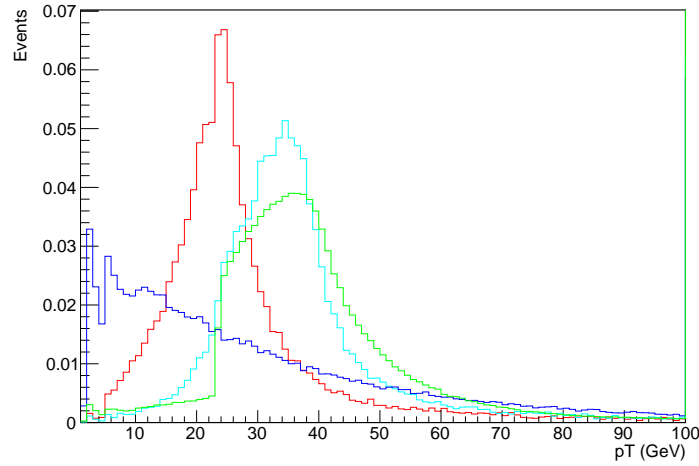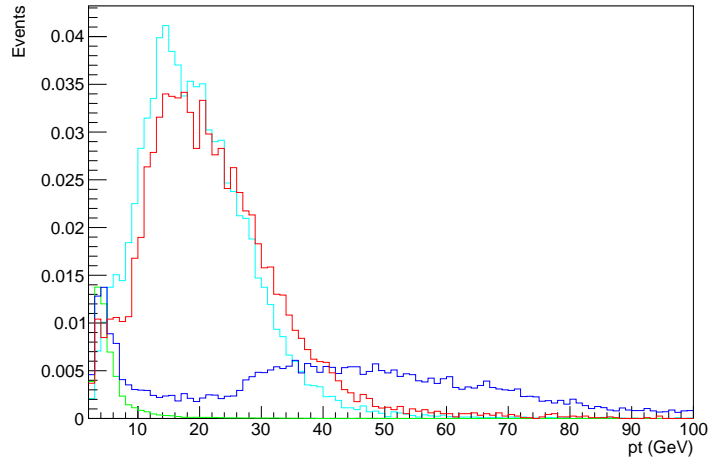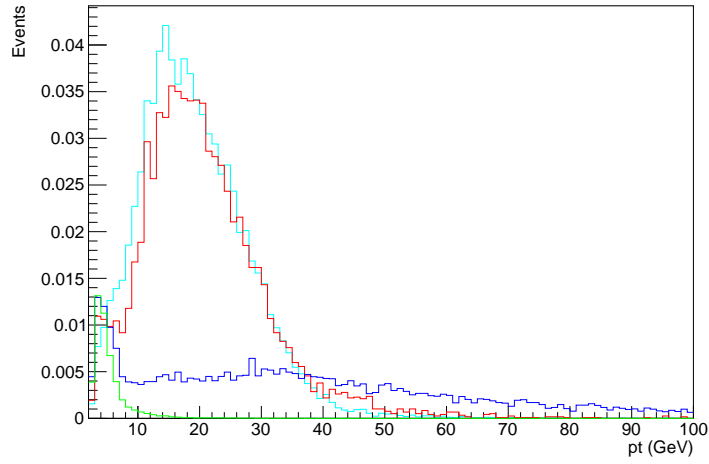

Figure 44: p_T distribution of muons for Majorana channel. Cyan is the distribution for the 20 GeV Majorana channel, red is the 50 GeV Majorana channel, blue is the $t\bar{t}$ background with Majorana criteria and green is the W$\mu\nu$ background with Majorana criteria
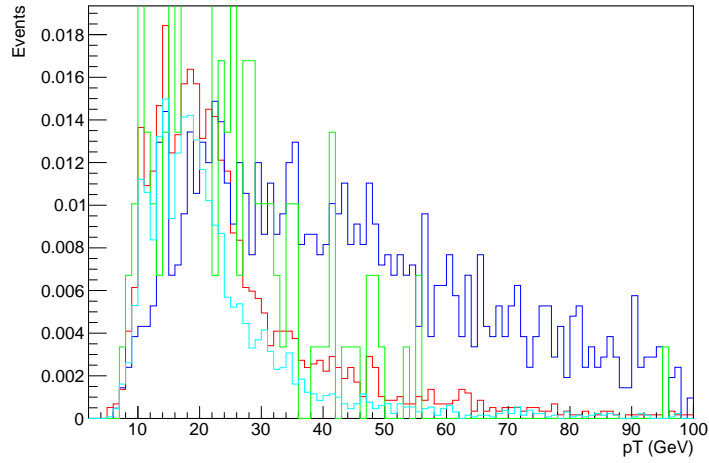
Figure 45: p_T distribution of electrons for Dirac channel. Cyan is the distribution for the 20 GeV Dirac channel, red is the 50 GeV Dirac channel, blue is the $t\bar{t}$ background with Dirac criteria and green is the W$\mu\nu$ background with Dirac criteria
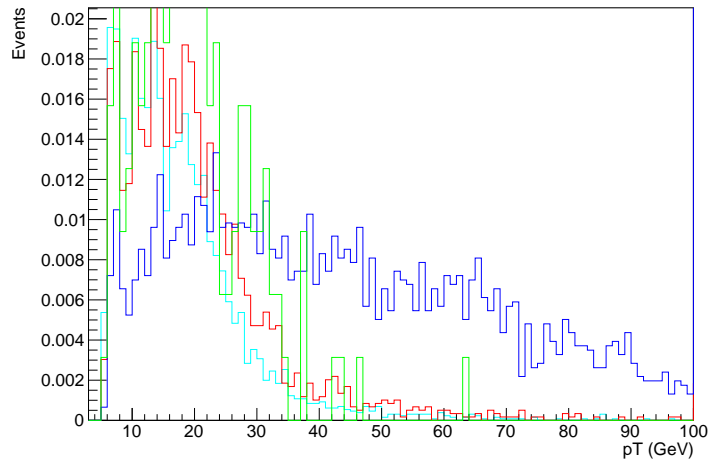

Figure 46: p_T distribution of electrons for Majorana channel. Cyan is the distribution for the 20 GeV Majorana channel, red is the 50 GeV Majorana channel, blue is the $t\bar{t}$ background with Majorana criteria and green is the W$\mu\nu$ background with Majorana criteria

Figure 47: p_T distribution of taus for Dirac channel. Cyan is the distribution for the 20 GeV Dirac channel, red is the 50 GeV Dirac channel, blue is the $t\bar{t}$ background with Dirac criteria and green is the $W\mu\nu$ background with Dirac criteria

Figure 48: p_T distribution of electrons for Majorana channel. Cyan is the distribution for the 20 GeV Majorana channel, red is the 50 GeV Majorana channel, blue is the $t\bar{t}$ background with Majorana criteria and green is the $W\mu\nu$ background with Majorana criteria
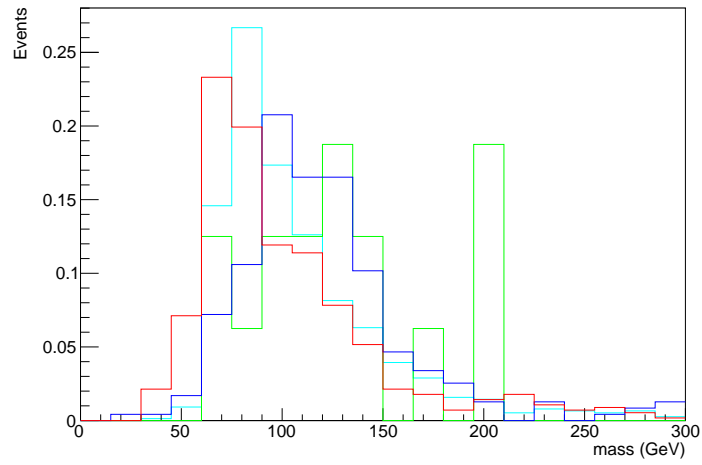
55

mass distributions

Figure 49: Reconstructed W masses. Cyan is the distribution for the 20 GeV Dirac channel, red is the 50 GeV Dirac channel, blue is the $t\bar{t}$ background with Dirac criteria and green is the W$\mu\nu$ background with Dirac criteria
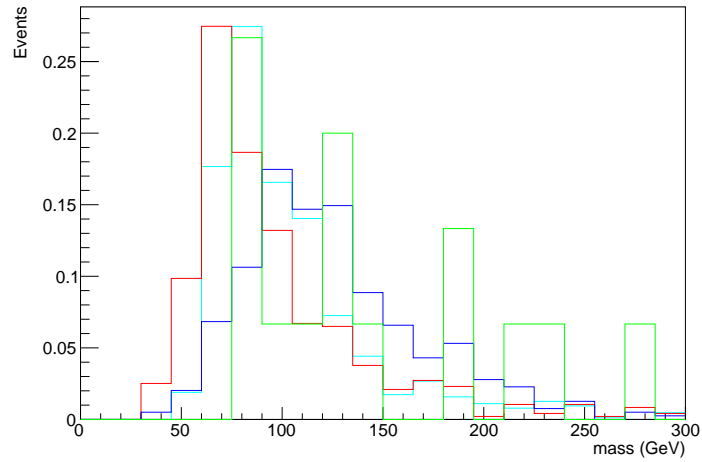

Figure 50: Reconstructed W masses. Cyan is the distribution for the 20 GeV Majorana channel, red is the 50 GeV Majorana channel, blue is the $t\bar{t}$ background with Majorana criteria and green is the W$\mu\nu$ background with Majorana criteria
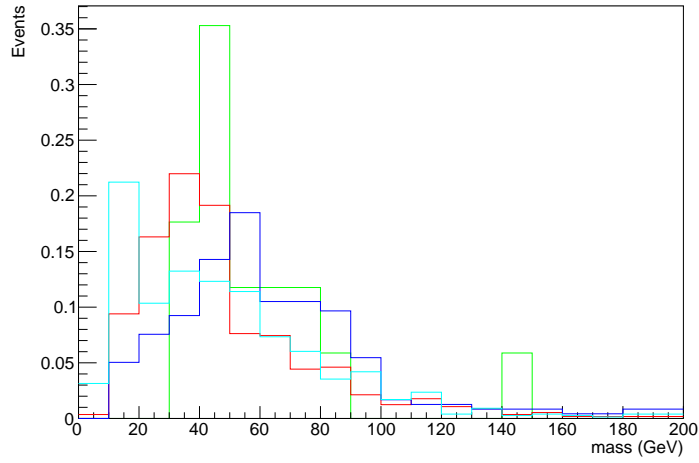
Figure 51: Reconstructed N masses. Cyan is the distribution for the 20 GeV Dirac channel, red is the 50 GeV Dirac channel, blue is the $t\bar{t}$ background with Dirac criteria and green is the W$\mu\nu$ background with Dirac criteria
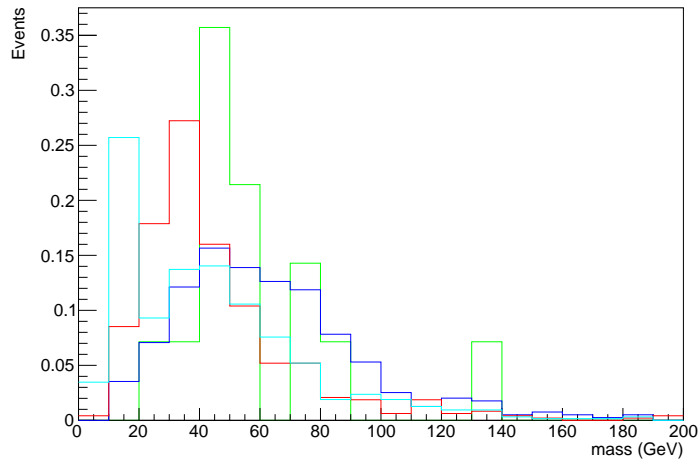

Figure 52: Reconstructed N masses. Cyan is the distribution for the 20 GeV Majorana channel, red is the 50 GeV Majorana channel, blue is the $t\bar{t}$ background with Majorana criteria and green is the W$\mu\nu$ background with Majorana criteria

List of files

Signal

For signal the ch1 files are the events which are referred to as Majorana channel throughout the thesis. Both ch2 and ch4 are the Dirac channel. The files are from both mc16a, mc16c and mc16d.

20 GeV

mc16_13TeV.800063.Py8EG_WmuHNL50_20G_lt01dd_tau_ch1.deriv.DAOD_SUSY3.e8102_e7400_a875_r9364_r9315 _p3990_tid21416718_00

mc16_13TeV.800063.Py8EG_WmuHNL50_20G_lt01dd_tau_ch1.deriv.DAOD_SUSY3.e8102_e7400_a875_r10201 _r10210_p3990_tid21416710_00

mc16_13TeV.800063.Py8EG_WmuHNL50_20G_lt01dd_tau_ch1.deriv.DAOD_SUSY3.e8102_e7400_a875_r10724 _r10726_p3990_tid21416692_00

mc16_13TeV.800064.Py8EG_WmuHNL50_20G_lt01dd_tau_ch2.deriv.DAOD_SUSY3.e8102_e7400_a875_r9364_r9315 _p3990_tid21416720_00

mc16_13TeV.800064.Py8EG_WmuHNL50_20G_lt01dd_tau_ch2.deriv.DAOD_SUSY3.e8102_e7400_a875_r10724 _r10726_p3990_tid21416714_00

mc16_13TeV.800064.Py8EG_WmuHNL50_20G_lt01dd_tau_ch2.deriv.DAOD_SUSY3.e8102_e7400_a875_r10201 _r10210_p3990_tid21416699_00

mc16_13TeV.800066.Py8EG_WmuHNL50_20G_lt01dd_tau_ch4.deriv.DAOD_SUSY3.e8102_e7400_a875_r9364_r9315 _p3990_tid21416716_00

mc16_13TeV.800066.Py8EG_WmuHNL50_20G_lt01dd_tau_ch4.deriv.DAOD_SUSY3.e8102_e7400_a875_r10201 _r10210_p3990_tid21416707_00

mc16_13TeV.800066.Py8EG_WmuHNL50_20G_lt01dd_tau_ch4.deriv.DAOD_SUSY3.e8102_e7400_a875_r10724 _r10726_p3990_tid21416705_00

50 GeV

mc16_13TeV.800075.Py8EG_WmuHNL50_50G_lt0001dd_tau_ch1.deriv.DAOD_SUSY3.e8102_e7400_a875_r10201 _r10210_p4164_tid21429397_00

mc16_13TeV.800075.Py8EG_WmuHNL50_50G_lt0001dd_tau_ch1.deriv.DAOD_SUSY3.e8102_e7400_a875_r10724 _r10726_p4164_tid21429443_00

mc16_13TeV.800075.Py8EG_WmuHNL50_50G_lt0001dd_tau_ch1.deriv.DAOD_SUSY3.e8102_e7400_a875_r9364 _r9315_p4164_tid21429438_00

mc16_13TeV.800076.Py8EG_WmuHNL50_50G_lt0001dd_tau_ch2.deriv.DAOD_SUSY3.e8102_e7400_a875_r10724 _r10726_p4164_tid21429452_00

mc16_13TeV.800076.Py8EG_WmuHNL50_50G_lt0001dd_tau_ch2.deriv.DAOD_SUSY3.e8102_e7400_a875_r10201 _r10210_p4164_tid21429447_00

mc16_13TeV.800076.Py8EG_WmuHNL50_50G_lt0001dd_tau_ch2.deriv.DAOD_SUSY3.e8102_e7400_a875_r9364 _r9315_p4164_tid21429400_00

Background

$t\bar{t}$

mc16_13TeV:mc16_13TeV.410470.PhPy8EG_A14_ttbar$_hdamp258p75_nonallhad.deriv.DAOD_SUSY3.e6337_s3126
_r9364_p3990

W$\mu\nu$

mc16_13TeV:mc16_13TeV.364156.Sherpa_221_NNPDF30NNLO_Wmunu_MAXHTPTV0_70_CVetoBVeto.deriv.DAOD
_SUSY3.e5340_s3126_r10724_p3990